2-14-2017

Catalysis in Real Time Using X-Ray Lasers

A. Nilsson
Stockholm University

Jerry L. LaRue
Chapman University, larue@chapman.edu

H. Öberg
Stockholm University

H. Ogasawara
SLAC National Accelerator Laboratory

M. Dell'Angela
CNR-IOM

See next page for additional authors

Catalysis in Real Time Using X-Ray Lasers

Authors
A. Nilsson, Jerry L. LaRue, H. Öberg, H. Ogasawara, M. Dell'Angela, M. Beye, H. Öström, J. Gladh, J. K. Nørskov, W. Wurth, F. Abild-Pedersen, and L. G. M. Pettersson

Chemical Physics Letters 675 (2017) 145–173

Contents lists available at ScienceDirect

Chemical Physics Letters

journal homepage: www.elsevier.com/locate/cplett

Frontiers article

Catalysis in real time using X-ray lasers

A. Nilsson [a,*], J. LaRue [b], H. Öberg [a,1], H. Ogasawara [c], M. Dell'Angela [d], M. Beye [e], H. Öström [a], J. Gladh [a], J.K. Nørskov [f,g], W. Wurth [e,h], F. Abild-Pedersen [f], L.G.M. Pettersson [a]

[a] Department of Physics, AlbaNova University Center, Stockholm University, SE-106 91 Stockholm, Sweden
[b] Schmid College of Science and Technology, Chapman University, One University Drive, Orange, CA 92866, USA
[c] SLAC National Accelerator Laboratory, 2575 Sand Hill Road, Menlo Park, CA 94025, USA
[d] CNR-IOM, Strada Statale 14 - km 163.5, 34149 Trieste, Italy
[e] DESY Photon Science, Notkestr. 85, 22607 Hamburg, Germany
[f] SUNCAT Center of Interface Science and Catalysis, SLAC National Accelerator Laboratory, 2575 Sand Hill Road, Menlo Park, CA 94025, United States
[g] SUNCAT Center of Interface Science and Catalysis, Department of Chemical Engineering, Stanford University, 443 Via Ortega, Stanford, CA 94305, United States
[h] University of Hamburg and Center for Free Electron Laser Science, Luruper Chaussee 149, D-22761 Hamburg, Germany

ARTICLE INFO

Article history:
Received 13 January 2017
In final form 7 February 2017
Available online 14 February 2017

ABSTRACT

We describe how the unique temporal and spectral characteristics of X-ray free-electron lasers (XFEL) can be utilized to follow chemical transformations in heterogeneous catalysis in real time. We highlight the systematic study of CO oxidation on Ru(0001), which we initiate either using a femtosecond pulse from an optical laser or by activating only the oxygen atoms using a THz pulse. We find that CO is promoted into an entropy-controlled precursor state prior to desorbing when the surface is heated in the absence of oxygen, whereas in the presence of oxygen, CO desorbs directly into the gas phase. We monitor the activation of atomic oxygen explicitly by the reduced split between bonding and antibonding orbitals as the oxygen comes out of the strongly bound hollow position. Applying these novel XFEL techniques to the full oxidation reaction resulted in the surprising observation of a significant fraction of the reactants at the transition state through the electronic signature of the new bond formation.

1. Introduction

The world faces many challenges over the next few decades concerning energy production, energy storage, and reduced energy impact on the environment. Nearly all chemical processes involved in energy conversion utilize catalytic chemical transformations at interfaces between solids and liquids or gases. These include novel electro- or photo-catalytic processes to produce hydrogen and to convert emitted CO_2 to fuels, more efficient and stable fuel cell catalysts and selective thermal heterogeneous catalytic processes generating methanol, higher alcohols and hydrocarbons. The chemical industry in the US is responsible for more than 10% of the US energy consumption [1], so it is important to develop a sustainable chemical industry. It has furthermore been estimated that the production of more than 90% of all these industrial chemicals is dependent on the availability of suitable catalysts, and that about 60% of all individual processes in the chemical industry rely on catalysis.

Many surface chemical reactions proceed through several elementary dynamical steps, which occur on different time scales. Fig. 1 shows a schematic reaction energy diagram going from reactants to products via different intermediates separated by various transition states where the highest barrier controls the kinetics of the overall process. The catalytic transformation from reactants to products is a rare stochastic event (typical turnover frequencies of a good catalyst is 1 per active site per second). Thus, if we monitor the various species on the surface using *in situ* techniques under steady-state conditions we might observe the adsorbed reactants and products and maybe also the first intermediate illustrated in the figure since the barrier for further reaction is rather high and therefore kinetically limited. However, the other intermediates will only be populated transiently due to their small activation barriers and the overall concentration at steady state conditions will be very low.

Today, most of our understanding of short-lived intermediates and the activation barriers separating them in heterogeneous catalysis comes from quantum chemical calculations [2], and it is essential that we complement this by suitable experiments. This means that we need experiments that can probe the more short-lived intermediates and the transition states on the relevant ultrafast time scales. Molecules at the transition state are extremely

* Corresponding author.
E-mail address: andersn@fysik.su.se (A. Nilsson).
[1] Present address: Department of Radioactive Materials, Swedish Radiation Safety Authority, SE-171 16 Stockholm, Sweden.

http://dx.doi.org/10.1016/j.cplett.2017.02.018
0009-2614/

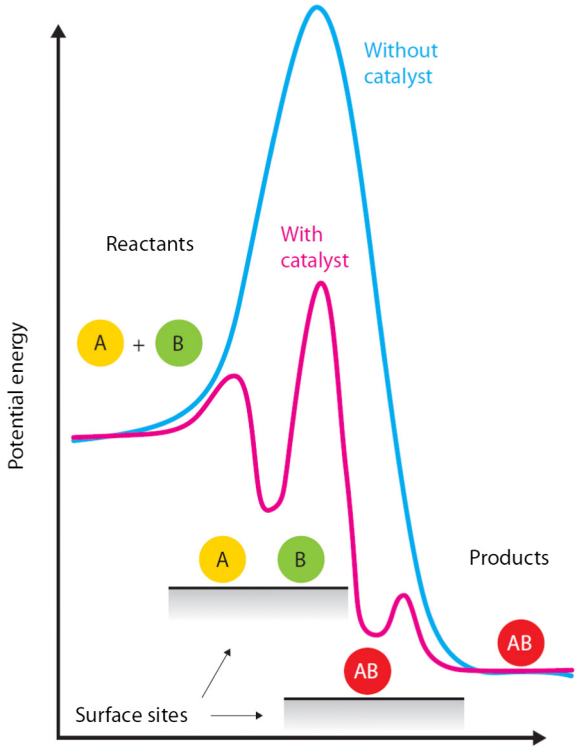

Fig. 1. Schematic picture of the potential energy surface of a gas phase reaction with a large barrier and more efficient surface catalytic reaction from reactants to products via two different intermediates and three smaller barriers [34].

hard to capture or observe due, not to a transient character, but rather to the near-zero instantaneous population at steady-state conditions. However, to achieve a complete understanding of the involved surface chemical reactions, we need detailed information on all steps in the dynamics of making and breaking bonds at the surface in terms of the individual atomic and molecular forces and the motions that these forces induce during chemical change.

Using an optical, ultrashort laser pulse we can increase the population of reactive species that will be turned into transient intermediates allowing for detection on an ultrafast time scale [3–10]. At metal surfaces the ultrashort laser pulses will interact with the metal substrate to excite electrons that then thermalize on a timescale of ~100 fs [11] and subsequently couple directly to the adsorbate system or via phonons to initiate a reaction [8]. Heating of the lattice is slower than of the electrons and during the first picosecond after laser irradiation there will be a strong non-equilibrium that can be utilized to deduce reaction mechanisms. Dynamics that are most efficient during the first picosecond are likely driven by excited electrons, whereas slower dynamics can also be phonon-driven. For reactions where the product is a gas phase molecule mass spectrometry two-pulse correlation techniques have been used to decouple electron- and phonon-mediated processes [8,12]. For instance, in CO oxidation on a Ru(0001) single-crystal, one of the prime model reactions for heterogeneous catalysis, the importance of electron- and phonon-mediated processes was studied [13]. Under thermal equilibrium and ultrahigh vacuum conditions CO desorbs molecularly from oxygen-covered Ru(0001). However the oxidation channel could be opened by femtosecond laser irradiation where extremely hot electrons can be produced on an ultrafast timescale and activate the adsorbed atomic O before the CO desorbs [13]. These experiments, however, did not provide information about the molecular interactions at the surface, or about active sites or intermediate species since only gas-phase products were probed. In order to get such information adsorbate-sensitive spectroscopic experiments are required.

Pump-probe spectroscopic experiments targeting surface reactions are technically challenging and have until recently only been performed on reversible transients, such as diffusion or trivial reactions like desorption. Vibrational sum-frequency generation (SFG) spectroscopy has been utilized in a number of studies due to the relative ease of time-resolving such experiments combined with the molecular specificity that vibrational spectroscopy provides. Reversible excitation of pre-dissociative NO on Ir(111) and diffusion of CO from step to terrace sites on a stepped Pt surface as well as simple reactions such as CO desorption from both Ru(0001) and Pt(111) have been studied with ultrafast SFG [4,14–17]. In these cases transient red-shifts of the internal CO stretching vibration were observed and these results were mainly discussed in terms of excitation of external vibrational modes, such as the frustrated rotation, during the desorption process.

Valence-band and core-level photoemission using higher harmonic generation of optical lasers have been used in pump-probe experiments to study the electronic structure changes in reversible transient phenomena [6,18]. The amount of information that could be extracted from such experiments has so far been limited due to the space charge issues involved in performing photoelectron spectroscopy with the presently available low repetition-rate intense femtosecond light sources; space charge issues arise if the removal of electrons leads to a build-up of an electrostatic potential that distorts the spectral features.

Synchrotron-based X-ray absorption spectroscopy (XAS) and X-ray emission spectroscopy (XES) have become the prime tools for investigating local electronic structure and chemical bonding of adsorbate systems under static conditions [19–22]. The most important properties of these techniques are their ability to provide element-specific and symmetry-selective information about the local electronic structure; the involvement of the very localized core-level results in a projection of the electronic structure onto the probed atom. In addition, XES can be used to selectively probe certain atoms of an element present at the surface if these have a distinct signature in XAS [23]. These core-level spectroscopies provide a way to measure adsorbate electronic structure in an element-specific and symmetry-resolved way and have been applied to a number of adsorbate systems [21].

Here we will present how such experiments can be extended to probe short-lived transient species during catalytic surface reactions. Fig. 2 illustrates how this can be achieved using an optical pump to initiate a reaction and X-ray pulses to probe the different reactants, various intermediates, and final products as they evolve in a sequential manner.

A prerequisite for time-resolved studies with X-ray probe pulses is that the time-duration of the pulses is shorter than the process under study and that they carry sufficient number of photons. New accelerator-based light sources, such as FLASH at DESY in Hamburg, Germany, the first free-electron laser in the extreme ultraviolet (XUV) and soft X-ray regime starting user operation in 2005 [24], the Linac Coherent Light Source (LCLS) at SLAC at Stanford, USA, the first hard X-ray laser world-wide [25], as well as SACLA at SPring-8 in Harima, Japan [26], also operating in the hard X-ray regime, and FERMI at Elettra in Trieste, Italy, the first fully externally seeded free-electron laser in the XUV regime [27], provide ultrashort XUV and X-ray pulses with pulse length on the order of a few femtoseconds to a few hundred femtoseconds with unprecedented brightness and coherence properties, see Fig. 3. With the European XFEL in Hamburg, the Swiss XFEL at PSI in Villigen, Switzerland and the PAL-XFEL in Pohang, Korea, three more XFELs are expected to produce first light by the end of 2016 and the beginning of 2017, respectively. These new light sources have

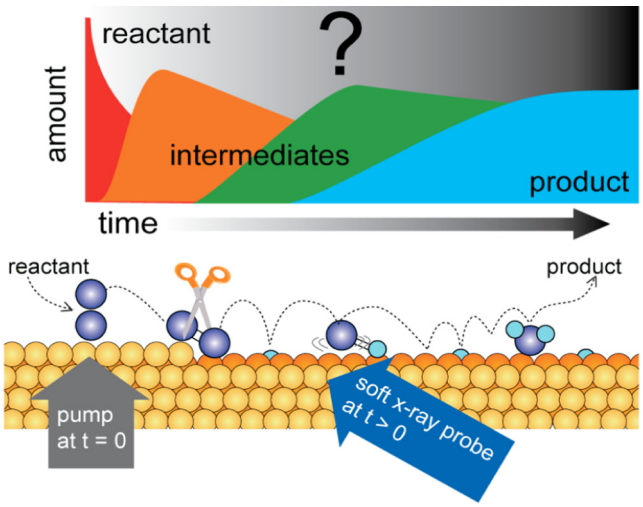

Fig. 2. Schematic picture of the elementary steps in a catalytic reaction involving molecular oxygen and hydrogen. The reaction is initiated by an optical laser pump and probed with an LCLS soft X-ray pulse. The concentration of reactants, various intermediates and products can be followed in real time.

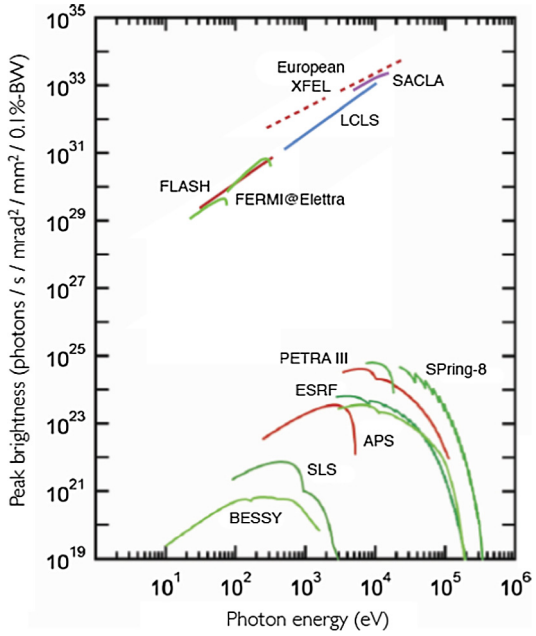

Fig. 3. Comparison of peak spectral brightness of storage ring and free-electron laser sources. Reproduced with permission from Huang et al. [35].

opened up many exciting new research opportunities in physics, chemistry and life sciences [28,29].

In the present review we will demonstrate how we can use the ultrashort X-ray pulses from X-ray lasers as exemplified by studies using the soft X-ray materials science (SXR) beamline at LCLS where the initial set of experiments has been conducted using XAS and XES. The focus is on CO and O on Ru(0001) and the different competing reaction pathways that open upon excitation of the system using either a 400 nm laser pulse or a novel concept of THz radiation [30]. To delineate the different processes we will describe separately the desorption of CO from clean Ru(0001), which results in population of a transient, entropy-based precursor state [31], and desorption in the presence of oxygen, in which case the specific interaction between O and CO eliminates the precursor state [32]. We will describe the activation of atomic oxygen which provides a particularly clear illustration of bonding and antibonding orbitals, measured in XES and in XAS, respectively, and how the split between them is reduced as the oxygen atom is activated and comes out from its equilibrium hollow position [33]. We finally combine and describe the different steps in the CO oxidation reaction on Ru(0001) where we, contrary to common expectation, could detect the electronic structure changes of molecules in the transition state region as they attempt to form the new O—CO bond [3]. At the end we also demonstrate how we can stimulate the CO oxidation reaction on Ru(0001) at room temperature selectively in comparison to CO desorption using THz radiation [30].

2. Experimental methodology

The introduction of XFELs that provide intense, ultra-short X-ray pulses has opened up new possibilities for studying chemical reactions at surfaces. Using time-resolved XAS and XES, snapshots of the electronic structure maps can be obtained as the reaction proceeds in time, revealing atomic- and site-specific intermediates and lifetimes. This information can be used to elucidate reaction pathways, branching ratios, and dynamics of important catalytic reactions. This multidimensional information is a unique aspect of these surface science X-ray laser studies. The focus in the present section will be to describe and discuss the different components that have been required to perform these experiments and to extract the maximum information.

2.1. Pump

The study of chemical dynamics requires the reaction of interest be initiated nearly instantaneously so that a common time zero is established and also a sufficient amount of the chemical species proceeds down the reaction coordinate in unison. This concerted excitation must be fast enough to allow the molecular motions, which are primarily responsible for reactivity, to be probed as a function of time during the critical steps of a chemical encounter. Femtosecond laser pulses on the same timescale or faster than molecular motions are ideal to pump these chemical reactions. The reaction dynamics can then be mapped out by probing the reaction as a function of time after laser excitation.

In the study of surface dynamics, specifically on metal catalysts, optical femtosecond lasers operating in the 800–400 nm range have been the workhorse of initiating chemical reactions [8]. The excitation process and relevant timescales are depicted in Fig. 4. During femtosecond excitation on metal surfaces, the electron bath of the surface absorbs the energy of the photons, creating a high-energy electron distribution that thermalizes in a few tens of femtoseconds. Due to electron-phonon coupling, the high-energy electrons decay into the phonon bath, heating it up while lowering the electronic temperature. After some picoseconds, the electron and phonon temperatures will thermalize to the same temperature. The electron and phonon modes can couple to and excite adsorbate motions on the surface. Electron-adsorbate coupling typically occurs on a sub-picosecond timescale by transient occupation of surface-adsorbate antibonding states, leading to rapid excitation of adsorbate nuclear motions. Phonon-adsorbate coupling, on the other hand, requires a few picoseconds after laser excitation for the phonon temperature to heat up and for the substrate phonons to couple to the adsorbate. The temperature of the electron bath, phonon bath, and adsorbate motions of CO on Ru(0001) are shown in Fig. 5 as a function of time after laser excitation. After the nuclear motions of the adsorbates are initially excited through either electron- or phonon-mediated processes, the reaction proceeds down the potential energy surface corresponding to a normal, thermally driven reaction.

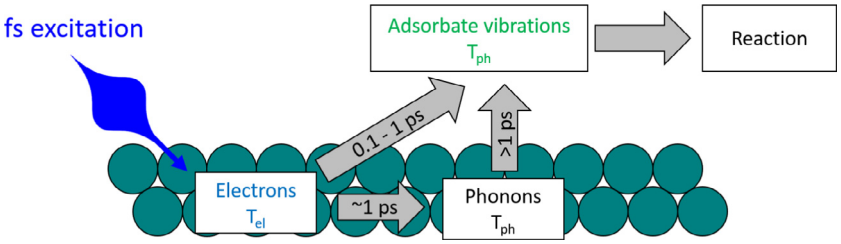

Fig. 4. Femtosecond initiation of a chemical reaction. The electron bath and the phonon bath of the surface can couple to the surface adsorbates, exciting nuclear motions and initiating reactions.

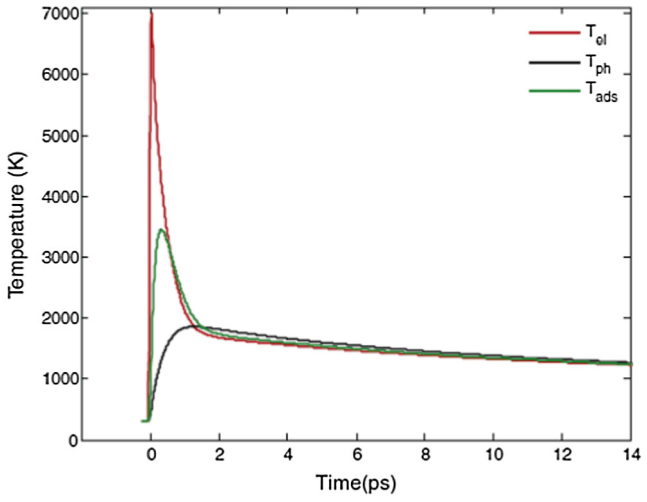

Fig. 5. Temperature of the ruthenium electron bath and phonon bath, as well as CO adsorbates, as a function of time after laser excitation. Reproduced with permission from Öberg et al. [36].

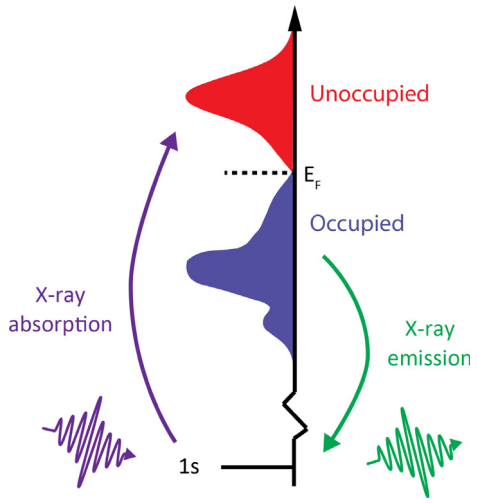

Fig. 6. Schematic showing the K-edge XAS and XES processes. In K-edge X-ray absorption, an X-ray excites an atomic core 1s electron to the unoccupied valence shell. An electron in the occupied valence shell relaxes to the atomic core, emitting an X-ray in the emission process.

For the experiments presented here, a 400 nm femtosecond pump laser with a temporal width of 70–100 fs was used to initiate the reaction [3,31,33]. The pump laser fluence ranged between 100 J/m^2 and 140 J/m^2, depending on the experiment, with higher laser fluences generally correlating to higher reaction yields.

2.2. Probe and set-up

Many electron-spectroscopic techniques, such as photoelectron spectroscopy, have severe limitations for ultrafast studies, since the large peak intensity builds up space charge on the surface which affects the electron energies [37–41]. XES and fluorescence-yield XAS are unique techniques used to probe the atom-specific electronic structure of a system that eliminate any space charge distortion as the excitation source and the detection both are based on photons. In the X-ray absorption process, a core electron in an atom is excited into an unoccupied orbital while the X-ray emission process takes place when the core hole of the excited atom is filled by a valence electron, as shown in Fig. 6. The core electron can only transfer to unoccupied valence states which have an overlap with the core state and the core hole can only be filled by an electron from an occupied valence shell in the proximity of the excited atom; both spectroscopies thus give a projection of the electronic structure onto the excited atom. The XAS spectra map out the unoccupied valence electronic structure while the XES spectra map out the occupied valence electronic structure of the bonding system. For the present studies, we used oxygen K-edge spectroscopy, where an O 1*s* core electron is excited into the valence electronic structure of the system in the X-ray absorption process.

XAS and XES in the soft X-ray region are dominated by dipole transitions and, together with the symmetry and character of the core-level, can thus provide important information about chemical bonding in an atomic site-projected manner similar to the linear combination of atomic orbitals (LCAO) approach in theoretical modeling. Performing resonantly excited XAS and detecting the subsequent emission, as in resonant inelastic X-ray scattering (RIXS) [42], leads to additional symmetry selection rules which further characterize the system [43]. Because of this, XAS and XES are powerful tools to investigate intramolecular bonds and adsorption of adsorbates on catalytic surfaces [21,44].

Soft X-ray free electron lasers (XFEL), which provide ultra-short X-ray pulses on the time scale of atomic motion, have opened up new possibilities for X-ray spectroscopies. The ultra-short X-ray pulses can be used in time-resolved XAS and XES to probe transient changes in the chemical bond breaking and formation processes on the femtosecond timescale during catalytic chemical transformations at surfaces and interfaces [3,31]. XAS and XES, when taken to this time-scale, give electronic structure snapshots as a function of time during the evolution of the chemical bonding, allowing for time-resolved energy maps. For example, Fig. 7 shows the XAS evolution for CO oxidation as a function of time. With these new advances, XFELs present the opportunity to monitor chemical reactions in a manner that is chemically and site-specific on the relevant ultrafast timescale. The time-resolution of the experiment is dependent on the inherent pulse widths of the pump source and

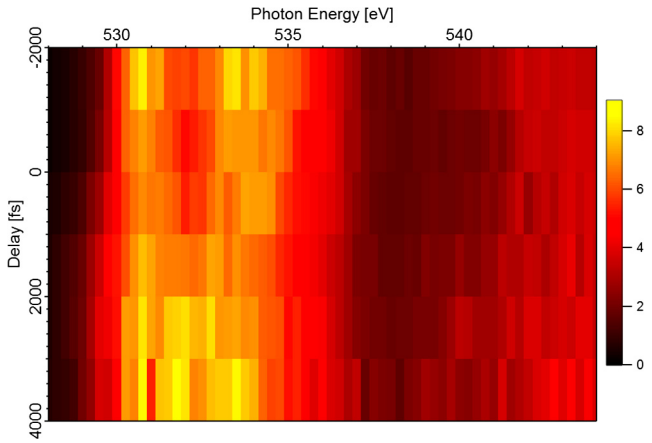

Fig. 7. The O 1 s XAS time evolution of CO oxidation on CO + O/Ru(0001). The reaction is initiated at t = 0 fs using a 400 nm femtosecond laser. The horizontal axis is the energy of the monochromatic X-ray photon probing the O $2\pi^*$ resonance of atomic O and CO during reaction conditions. Before laser excitation, the O $2\pi^*$ resonance of atomic O (531 eV) and CO (534 eV) are distinguishable. After laser excitation, significant changes arise in the O $2\pi^*$ resonance, such that the atomic O and CO O $2\pi^*$ resonances are no longer distinguishable. This is a result of significant interaction between mobile O and excited CO on the Ru(0001) surface [3].

XFEL probe, as well as the relative timing between them. The relative timing between the pulses can be monitored down to sub-100 fs resolution for each shot using a non-destructive optical X-ray cross-correlator [45].

The optical pump/X-ray probe experiments presented here were performed using the surface science endstation (SSE) [46] at the soft X-ray hutch (SXR) at the LCLS at the SLAC National Accelerator Laboratory. For more detailed information regarding the SXR beamline, please refer to reference [47]. Fig. 8a shows a typical configuration of SSE for ultrafast studies of surface reactions using soft XFEL-based XAS and XES. The SSE consists of preparation and analysis vacuum chambers. The preparation chamber is equipped with standard ultra-high vacuum surface science instruments, such as an ion-gun for sample cleaning and a gas introduction system for sample preparation. The analysis chamber is equipped with a grating-based wavelength-dispersive spectrometer for partial fluorescence-yield XAS and XES measurements and an electron-energy analyzer for photoelectron spectroscopy measurements [46]. The SSE geometric configuration shown in Fig. 8b allows independent rotation of the sample to permit arbitrary angles between the X-ray **E**-vector and the sample surface, and any choice of detection angle with respect to the sample surface for (polarization-dependent) XAS measurements as well as for (polarization-dependent) symmetry-selective XES. The sample is mounted on a sample holder at grazing angle (~1–3°) with respect to the incoming XFEL light.

Grazing incidence geometry is preferred since this enhances the illuminated surface as well as reduces sample damage by increasing the reflectivity of the metal and dispersing the beam spatially over the surface to reduce the flux density. The peak power produced by XFELs can damage the catalytic surface under study [46]. When the metal substrate absorbs intense X-rays from the XFEL on a sub-100 fs time scale, the production of a secondary electron cascade can result in the ablation of several atomic layers near the surface [48]. These electrons can disrupt the system by dissociating or desorbing the surface species under study. If the core ionization event occurs more frequently than the decay event of the core holes then double core hole creation can lead to the probed electronic structure being modified during the duration of the X-ray pulse. In particular, high peak intensities exceeding 10^{17} W/cm^2 can induce double core ionization, which gives rise

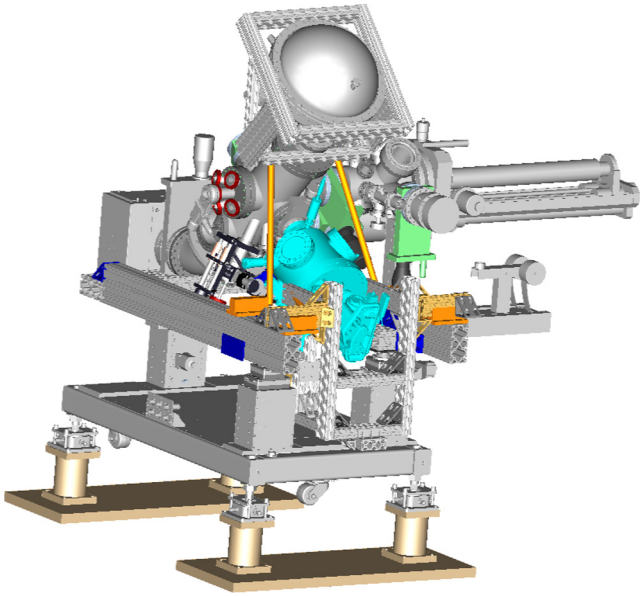

Fig. 8a. The surface science endstation set-up for optical pump and X-ray probe XAS and XES measurements. The system runs under ultra-high vacuum conditions. The system is equipped with a soft X-ray grating spectrometer and an electron spectrometer. The shown configuration includes a manipulator which allows the sample to be rotated along the beam axis and also allows positioning and transfer of the sample between the preparation chamber and the analysis chamber.

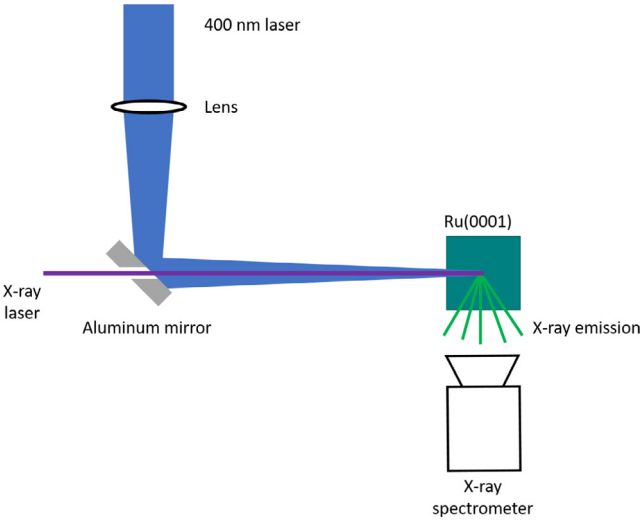

Fig. 8b. Schematic of the optical laser pump, X-ray laser probe experiment setup. The 400 nm optical and X-ray lasers are co-linearly coupled. The X-ray spectrometer energy-resolves the emitted X-rays to create XAS and XES spectra.

to X-ray emission in a completely different energy region. To confirm the absence of such electronic structure damage, we compared XAS and XES measured at the XFEL to that measured at a synchrotron radiation facility where the peak intensity is much lower [46].

2.3. X-ray Free Electron Lasers (XFEL)

With the exception of FERMI, the free-electron lasers currently in operation in the VUV and X-ray range are based on 'Self-Amplified Spontaneous Emission' SASE. This process occurs when ultrashort, high-current, low-emittance electron bunches from a linear accelerator enter long periodic magnetic structures with

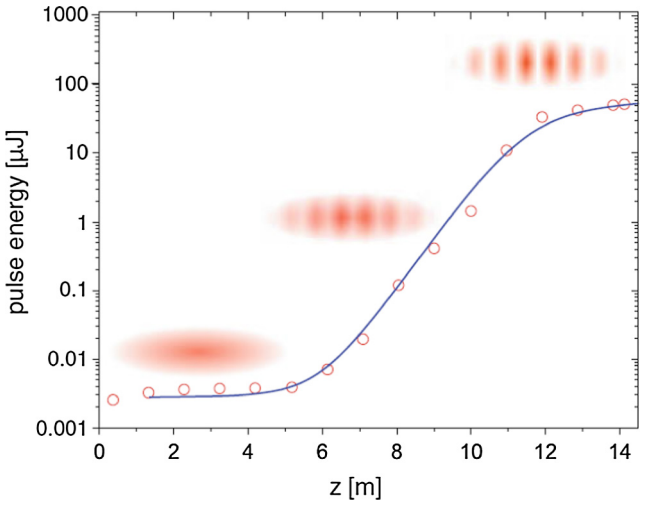

Fig. 9. The exponential growth of the XFEL pulse energy as a function of the distance z that the electron bunch traveled in the undulator. The cartoons show the growing density modulation of the electron bunch. The data (open circles) were obtained in the early days of FLASH [49].

alternating magnetic poles, so-called undulators, where they start to emit electromagnetic radiation at a specific wavelength $\lambda = \frac{\lambda_u}{2\gamma^2}\left(1+\frac{K^2}{2}\right)$, where λ_u is the period of the magnetic structure, $\gamma = \frac{E}{m_0c^2}$ is the relativistic ratio of the electron energy to its rest mass energy, and K is the so-called undulator parameter which depends on the magnetic field at the position of the electron beam and is on the order of 1. Wavelength changes can be achieved by either changing the electron beam energy or varying K that modifies the on-axis magnetic field which is usually done by changing the distance of the magnetic poles perpendicular to the beam. If the emitted electromagnetic radiation acts back on the electron bunch in a long undulator this leads to a density modulation of the electron bunch with a period equal to the wavelength of the emitted radiation. Electrons that are microbunched in this way start to emit in phase which leads to an exponential growth of the radiation field along the undulator until saturation is reached (see Fig. 9). Coherent emission from the electrons in the bunch leads to the very high peak brightness as well as to the high degree of transversal coherence of the XFEL sources in comparison to storage ring sources where the emitted radiation from individual electrons adds incoherently. Temporally SASE sources are not fully coherent since the amplification process in a SASE XFEL starts from noise that typically leads to several longitudinal modes in the radiation field [49]. Startup from noise then also results in shot-to-shot, *i.e.* pulse-to-pulse, fluctuations of pulse energy, pulse duration and photon energy. In many cases these fluctuations imply that it is necessary to record and store experimental data on a shot-to-shot basis and sort the data afterwards according to the simultaneously recorded photon pulse parameters which in turn requires sophisticated single-shot photon diagnostics.

For the time-resolved X-ray spectroscopy experiments discussed in this review the fluctuations in photon energy which are typically on the percent level would severely limit the resolution of the experiments. Since element-specific electronic-structure studies will typically require a relative photon bandwidth $\frac{\Delta\lambda}{\lambda} \leqslant 10^{-1}$ this results in the need to monochromatize the SASE radiation. For this purpose at LCLS the SXR beamline [47,50] has been built which covers the soft X-ray spectral regime accessible at LCLS. One drawback of using a monochromator to decrease the bandwidth of SASE radiation is an accompanying increase in pulse energy fluctuations [51]. Besides the photon energy and pulse energy fluctuations encountered at a SASE XFEL also the timing jitter between the pump pulses, which are usually derived from an external albeit synchronized optical laser, and the XFEL plays an important role for time-resolved X-ray spectroscopy experiments. Without corrections that require single-shot analysis of the relative arrival time of the two pulses the time resolution of pump-probe experiments would be typically limited to more than 200 fs at SASE sources such as LCLS. However, based on early proof-of-principle experiments performed at FLASH [52,53] single-shot cross-correlation methods based on transient X-ray induced optical reflectivity changes in semiconductors have been developed which allow correcting for the timing jitter between optical (pump) laser pulses and XFEL (probe) pulses [45,54]. It should be noted that neither monochromatization nor correction for timing jitter is necessary when a fully externally seeded XFEL is used as is now available for low energies at FERMI [27].

3. Theoretical simulations

The close synergy between theory and experiment is a characteristic of the studies that are presented here. It is clear that only through this combination has it been possible to extract the full extent of information from the experimental data, *e.g.*, assignment and characterization of the precursor state in CO desorption [31], the absence of a precursor state in CO desorption in the presence of coadsorbed oxygen [32] and catching the reacting molecules in the transition-state region [3]. Here we will discuss some of the theoretical and modeling aspects of this synergy.

3.1. The d-band model

The *d*-band model of Hammer and Nørskov [55] is illustrated schematically in Fig. 10 as a step-wise development of the bond between an adsorbed molecule and the metal surface. Initially, on the left side of the illustration we have the molecule in gas phase with a rather well-defined valence level that will eventually interact with the substrate. On the right hand side we have the electronic structure of the metal with a broad and featureless *sp* conduction band and a more narrow and well-defined *d*-band. Since it is a metal, the *sp* conduction band is half-filled and, for a transition metal, the *d*-band crosses the Fermi level, or lies near it, so also here there are empty states.

If we imagine that we turn on the interaction between adsorbate and metal first with the *sp*-band we will basically find a broadened adsorbate level. Coupling this broadened level to the *d*-band leads to the formation of bonding and antibonding states where the strength of the resulting bond will depend on the degree of filling of these levels; the energy position of the *d*-band will be decisive here. If the *d*-band is high in energy then mainly the bonding states will be populated as the antibonding ones will be pushed up above the Fermi level. For a system with lower-lying *d*-band, the antibonding states will be more filled as they are pulled down below the Fermi-level and this will compensate much of the bonding interaction and lead to weaker bonding. The *d*-band center has thus turned out to be a good descriptor in comparing chemisorption energies between different metals where linear relations, so-called scaling relations, are found to describe reaction energies as well as reaction barriers [56,57].

3.2. Computational

Common to all the studies discussed in the present review is the Ru(0001) substrate which was modeled either by using a fully periodic slab model or by cutting out a small, 17 atoms, cluster to represent the extended surface in some of the spectrum calcula-

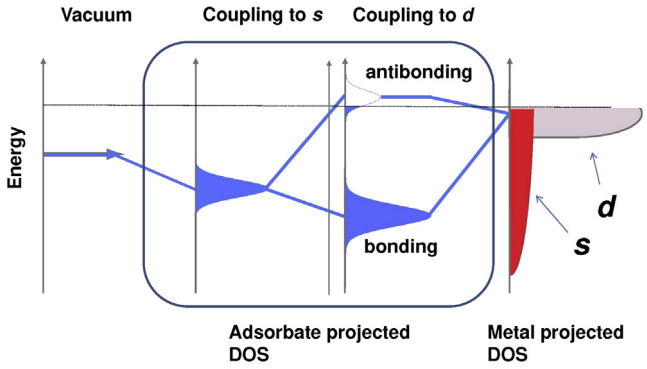

Fig. 10. Schematic illustration of how an adsorbate level (left) forms bonding and antibonding states with the *d*-band of a transition metal with occupation and splitting which is specific to the metal and characteristics of the site. The interaction with the much broader *sp*-band is more generic and similar for all metals and leads more to a broadening of the adsorbate level.

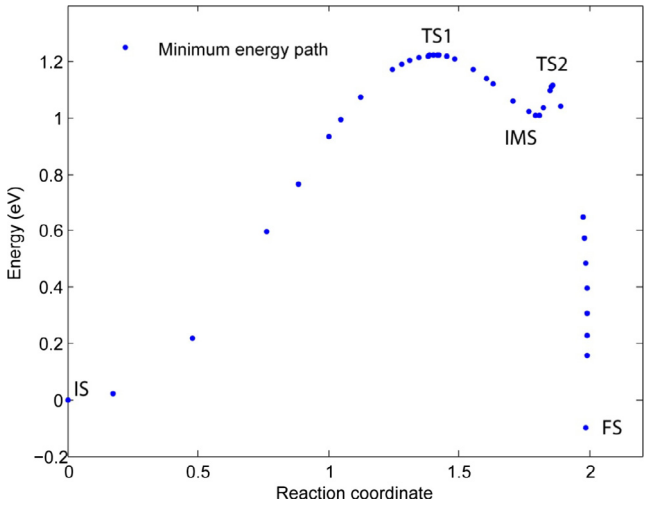

Fig. 11. Minimum energy path of CO oxidation on Ru(0001), from initial state (IS), in which CO and O are coadsorbed in the honeycomb phase of O. The reaction mediates over transition state 1 (TS1) leading to the formation of an intermediate state (IMS) of adsorbed CO_2 which is adsorbed with a small barrier (0.12 eV passing TS2) against gas phase (FS).

tions. Considering first the slab models of the Ru(0001) substrate, they typically consisted of 3–4 atomic layers where the bottom 1 or 2 layers were kept fixed in the experimental geometry while all other degrees of freedom were relaxed since the purpose was to model the extended system. The density functional theory (DFT) calculations on the slab models were performed using either the GPAW code [58,59], which is a real-space, numerical grid-based program, or the Quantum Espresso code [60] when performing free-energy calculations and *ab initio* molecular dynamics (AIMD) simulations, which uses a plane wave basis set.

For the studies of CO desorption from clean Ru(0001) a 2×2 cell with periodic boundary conditions was used in which a CO molecule was adsorbed at the ontop site corresponding to a coverage of 0.25 ML. From the top of the CO molecule to the bottom of the adjacent slab, a separation of 10 Å of vacuum was employed in the surface normal direction; a sufficient amount of vacuum between slabs is important in order to avoid artifacts. The DFT calculations of the potential energy surface of CO desorption were performed using the BEEF-vdW exchange-correlation (XC) functional [61], which includes van der Waals (vdW) interactions. This longer-range interaction is very important and decisive for determining the potential at the distances which support the precursor state. Starting at a C—Ru distance around 3.5 Å, we find an attractive plateau which, as we shall see from the potential of mean force (PMF), is essential in the theoretical interpretation of the experimental results for CO desorption and the precursor state.

The determination of the minimum energy path (MEP) for CO oxidation and CO_2 desorption using NEB-CI (nudged elastic band-climbing image) [62] required particular care due to the very different characters of the first and final parts of the path (Fig. 11). Initially, six intermediate images were employed in the method after which segments of the generated path were selected and more images were added to ensure localization of the true transition state. In total, the MEP from the initial state (IS) to the intermediate state (IMS) contains 22 intermediate images. In addition, the vibrational frequencies of the first transition state (TS1) generated with NEB were calculated to verify that the obtained configuration contained only one imaginary frequency. The second part of the MEP, the CO_2 desorption from IMS to the final state (FS), was challenging to obtain and was calculated using constrained optimization, where the C—Ru distance was kept fixed upon stepwise displacing the CO_2 molecule out from the surface along the surface normal. Around the curvature surrounding the second transition state (TS2) a reduced step size of 0.01 Å was employed to estimate the transition state geometry accurately. Note, however, that this approach may still lead to a slight overestimation of the barrier since the force minimization in each constrained optimization yields a local minimum so that the estimated TS2 is not necessarily the true saddle point on the potential energy surface (PES) but rather a local minimum in its vicinity.

3.3. Free-energy calculations

The free energy along the MEP of the reactions determined for the surface species from the NEB-CI method [62] was obtained based on frequencies in a harmonic oscillator approximation using the thermochemistry python package available in the Atomic Simulation Environment (ASE) [63]; the ASE contains a large variety of applications for building models and for analyzing results. In this approach, the degrees of freedom of the reacting adsorbates are assumed to be represented by localized oscillators with only vibrational modes. The vibrational mode that corresponds to the reaction coordinate, *i.e.* the one with a frustrated CO rotation and O translation in the CO oxidation study [3] (shown in Fig. 12), was excluded in the free-energy profile calculation.

As a practical example of these free-energy calculations we will discuss the desorption of CO from Ru(0001) [31] where we also found the largest contribution from entropy. We assume that the potential energy is separable in translational and rotational degrees of freedom

$$\begin{aligned} V_{tot} &= V_0 + V_x + V_y + V_{rot1} + V_{rot2} \\ &\approx V_0 + 2V_{trans} + V_{rot1} + V_{rot2} \end{aligned} \quad (1)$$

where the rotational potentials (V_{rot1} and V_{rot2}), translational potentials parallel to the surface (V_x and V_y) and the potential of the MEP (V_0) have been introduced. The high-frequency internal CO stretch vibration is neglected, since it is assumed to not be excited. On the right hand side of Eq. (1) it is also assumed that the two translational degrees of freedom on the surface are equivalent. As proposed by Doren and Tully [64,65] the PMF, $W(s)$, can be written as

$$W(s) = -k_B T \ln(g(s)) + k_B T \ln(g(\infty)), \quad (2)$$

where k_B is Boltzmann's constant, T is the temperature, s is the distance from the surface to the center of mass of the CO molecule and $g(s)$ is given by the integral

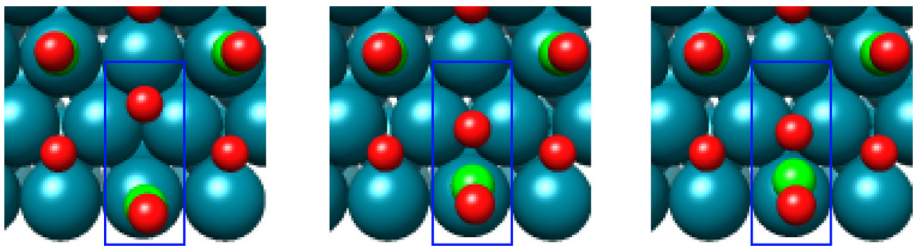

Fig. 12. Illustration of the vibrational mode excluded from the free energy profile calculation. This corresponds to the MEP in the CO oxidation reaction.

$$g(s) = \Gamma^{-1} \int e^{-\frac{V(s,\mathbf{q})}{k_B T}} d\mathbf{q} \tag{3}$$

here **q** represents the four degrees of freedom (two rotations and two translations orthogonal to the path of desorption) and Γ is an arbitrary normalization constant, the choice of which is irrelevant when the PMF is set to zero at infinite separation through Eq. (2).

Inserting Eq. (1) into Eq. (3) the following is obtained:

$$\begin{aligned} g(s) &= \Gamma^{-1} \int e^{-\frac{V_0(s)+2V_{trans}(s,x)+V_{rot1}(s,\theta)+V_{rot2}(s,v)}{k_B T}} dx d\theta dv \\ &= \Gamma^{-1} 2 g_{trans}(s) g_{rot1}(s) g_{rot2}(s) \end{aligned} \tag{4}$$

By adding and subtracting V_0 to each degree of freedom, the PMF can be written as a correction for each degree of freedom

$$W_{tot}(s) = V_0 - \sum_i^N (W_i - V_{0,i}^{fit}) \tag{5}$$

where V_0 is the energy of the MEP (effectively the *z*-direction), W_i is the PMF and $V_{0,i}^{fit}$ is the fit to V_0 for the ith degree of freedom. $V_{0,i}^{fit}$ only differs from V_0 to the extent that our mathematical representation of the potential in this direction is approximate. By subtracting it out in each degree of freedom, this error, however, is cancelled out.

To calculate the individual contributions, the degrees of freedom were sampled by calculating the potential energy of the two rotations (cartwheel and helicopter) and a translation of the CO molecule at fixed surface distances using the BEEF-vdW exchange-correlation (XC) functional. The potential energy curves for each degree of freedom were then fitted to functions for each surface distance and inserted in the integral in Eq. (4).

3.4. AIMD simulations

To better understand some of the mechanistic aspects of the surface reactions at elevated temperatures we employed AIMD to simulate the dynamical evolution of the systems of interest. The AIMD simulations at absolute temperature T = 2000 K were all carried out in the canonical ensemble. The dynamics at a controlled temperature is obtained by solving the Langevin equation as implemented in the ASE [63]. In the Langevin dynamics, all particles receive a random force through coupling to the heat bath and all particles have their velocities lowered through a constant friction term. This happens at every time step in the simulation under the restriction that the fluctuation-dissipation theorem is obeyed, which in turn ensures the statistics of the canonical ensemble. The friction in our simulations was set at 0.002 a.u. and the velocities of the atoms in each system were initialized according to a Boltzmann distribution at 3000 K and allowed to thermalize to 2000 K through energy transfer defined by the electronic friction. The time for thermalization was 1 ps and the trajectories for that time period were discarded from the analysis. Sufficiently large unit cells ($2 \times 4 \times 3$) of the optimized CO/Ru (0001) and 2O + CO/Ru(0001) structures were used to avoid dynamical constraints in the simulations. Interatomic forces were obtained on-the-fly from Quantum Espresso using the BEEF XC functional at 500 eV energy cutoff and a $6 \times 3 \times 1$ ***k***-point sampling of the Brillouin zone. Simulations were run until desorption of CO from the surface was achieved.

3.5. Constrained Space Orbital Variation (CSOV) analysis

In comparing the desorption of CO from the clean Ru(0001) surface and in the presence of coadsorbed oxygen it was important to analyze the differences in bonding and in particular to quantify the differences in the interaction at longer range. For this a CSOV analysis [66] was employed which allowed identifying the reduced repulsion between the CO 5σ and the *sp*-density at the surface in the case of coadsorption with oxygen as the main difference between the two situations.

The CSOV analysis starts with well-characterized CO molecular and surface model orbitals (here a Ru_{17} atom cluster) obtained by computing the system with CO at large distance from the surface. The orbitals are characterized in terms of belonging either to the cluster or to CO and whether they are occupied or empty. The system is then brought into contact, but when the Kohn-Sham matrix has been constructed it is transformed to the MO basis after which one can allow or disallow specific orbital interactions by simply making zero the corresponding off-diagonal Kohn-Sham matrix elements.

In the case of the desorption studies we were interested in the initial repulsion and thus disallowed any mixing between CO and metal and between occupied and unoccupied orbitals. The comparison with the fully relaxed system at large separation and the energy obtained without allowing orbital relaxations then gave the initial repulsion in each case; this initial repulsion can then in the CSOV analysis be stepwise overcome, *e.g.*, by first allowing mixing between occupied CO and unoccupied metal orbitals, corresponding to charge transfer from CO to the metal. In a second step back-transfer from the metal to CO can be included by allowing occupied metal states to mix with unoccupied CO orbitals. Extending step by step the orbital spaces that are allowed to interact and mix, one arrives finally at the fully relaxed solution, but with a decomposition of the energetic contributions to the bonding according to their importance. In the comparison of CO interacting either with clean Ru(0001) or O/Ru(0001) the initial repulsion was found to be smaller for the coadsorbate system. This can be understood by considering how CO binds to a metal, which is best described in terms of π-bonding and σ-repulsion [67–70]. When CO adsorbs on-top of a metal atom, electron density on the metal needs to be moved away to minimize the Pauli repulsion with the closed-shell CO 5σ lone-pair. Oxygen adsorbed on the surface withdraws charge from its surrounding metal atoms and thus reduces the repulsion with the lone-pair. As a result, the

interaction becomes more directional farther out in the van der Waals plateau with a resulting loss of entropy [31].

3.6. Simulations of X-ray spectra

Another key modeling aspect is the computation of X-ray spectra to aid in the analysis and interpretation of the experimental features. Both XES and XAS have been implemented in GPAW [71]. For XES the ground state orbitals are used which entails neglecting relaxation effects due to the core hole in the intermediate state as well as due to the valence hole in the final state [72]. To compare with the experimental spectra a broadening with a Gaussian function of 1 eV at full-width half-maximum (FWHM) was employed. To obtain an absolute energy scale the computed spectra were shifted to align the energy position of the CO $1\tilde{\pi}$ state with that of the corresponding experimental spectrum; the tilde ($\sim$) sign indicates that the original gas-phase 1π molecular orbital on CO has been modified through the interaction with the substrate.

O K-edge XAS spectra and core-excited state wave functions for CO in the precursor state were obtained using the StoBe-deMon [73] DFT code using a three-layer cluster model containing 17 Ruthenium atoms to represent the Ru(0001) surface. Spectra were computed within the transition-potential approach of Triguero et al. [74,75] The energy scale was adjusted by shifting the spectrum at the chemisorbed equilibrium geometry to have its $2\tilde{\pi}^*$ peak aligned with that of the unpumped experiment; the same shift was then applied to all other spectra. The XAS calculations used the exchange by Becke [76] and the correlation functional by Perdew [77]; it has been shown [75,78], however, that the spectral shape does not depend significantly on the choice of functional. A Gaussian broadening of full-width-at-half-maximum 0.5 eV was applied up to 534 eV and then linearly increased to 3 eV until 539 eV and constant beyond that.

To indicate the reliability of these spectrum calculations Fig. 13 shows a direct comparison between the experimental and computed XAS spectra of adsorbed CO and O as pure adsorbate phases on Ru(0001) for which the structure is well known; these spectra were computed using GPAW and the half-core-hole transition potential approach [71,74,75]. The adsorbed O phase has some minor impurities of CO contributing to the experimental spectrum.

4. CO dynamics on Ru

The making and breaking of surface-molecular bonds are the simplest, but undoubtedly also the most important surface processes in heterogeneous catalysis. Getting a glimpse of the transition between a surface-bound molecule and its gas phase equivalent has been at the top of surface scientists' wish list for as long as the field has existed. With the improvement of ultrafast laser-based techniques we can now access the short time-domains of surface transformations of a physicochemical nature and obtain better understanding of the underlying dynamics of desorption processes. Here we will focus on the most commonly studied molecule, namely CO, and use as substrate Ru. The system will also be extended to CO desorbing from Ru(0001) with co-adsorbed O where the presence of oxygen has a significant effect on the CO desorption dynamics.

However, since we will monitor the processes through changes in the electronic structure of surface-bound CO, we first need to discuss the binding of CO to a metal. The common frontier-orbital picture of σ-donation and π^* back-donation does not describe the new states that are formed and we thus need to revise the picture of the CO-metal bond.

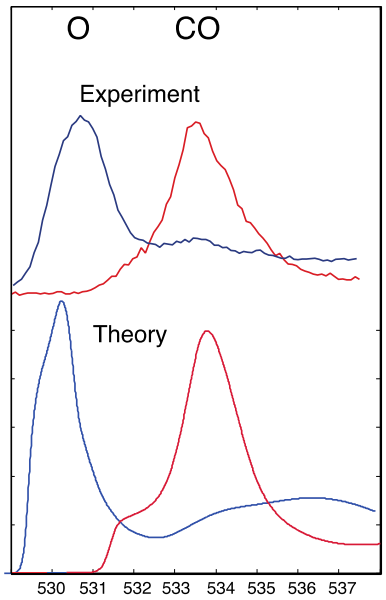

Fig. 13. Experimental (top) and computed (bottom) XAS spectra of CO on Ru(0001) and O on Ru(0001) showing excellent agreement. The intensity between 533 and 534 eV in the experimental spectrum of O on Ru(0001) is due to some minor CO contribution.

4.1. CO surface chemical bonding

Here we will thus first review the nature of the chemical interaction of CO on Ru(0001) in terms of the electronic structure and how this manifests in terms of signatures in XES and XAS [20,21,70,79]. The molecule bonds in a perpendicular geometry with the C end down and coordinates to one Ru atom in on-top position [21]. Fig. 14 shows on the left the XES and XAS spectra of CO interacting with a Ru surface and the corresponding DFT calculated molecular orbitals on the right, which are further compared with the free CO gas phase orbitals. We start with the π-interaction which, in the allylic configuration involves one metal atomic *d*-orbital and a 2*p* orbital from each of the C and O atoms leading to three molecular orbitals being generated [68,69,79]. The lowest orbital is bonding between all atomic centers and resembles the 1π orbital in gas phase CO which, due to the difference in electronegativity between C and O, is polarized towards the oxygen end of the molecule; through the attractive interaction with the metal the lowest orbital shifts density towards the C to enhance the bonding overlap with the metal *d*-state. The middle orbital has to contain a node since the wave function changes sign at the two end atoms making these antibonding with respect to each other. This creates a lone-pair orbital on the oxygen atom with no contribution on the carbon atom. Since the orbital is dominated by the substrate *d*-band contribution it is denoted $\tilde{d}_\pi$. The highest orbital is antibonding between all three centers and thereby closely resembles the $2\pi^*$ orbital seen in gas phase CO. Although these orbitals are created upon the absorbate-substrate interaction another question is how the original CO orbitals are rotated to obtain this allylic configuration. It has been shown that we can understand this as mixing of the gas phase CO 1π and $2\pi^*$ orbitals which can be understood as partly breaking up the π-bond within the molecule and generating virtual radical orbital states on either the C or O atoms. The effect on the C atoms of the interaction with the metal *d*-states can be described similarly as within the *d*-band model while on the O atom it generates the lone-pair state.

The σ-interaction has, on the other hand, been shown to be repulsive in nature at the short distance required for π-bonding

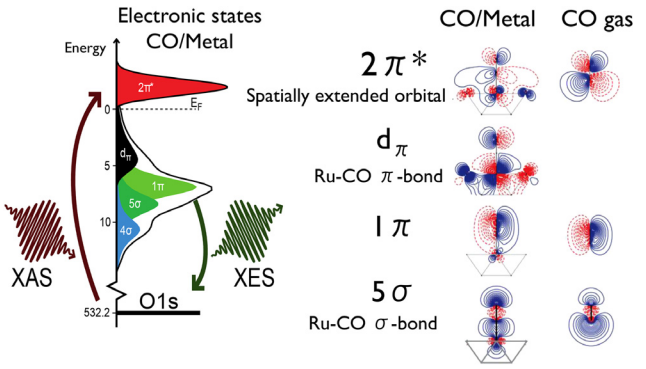

Fig. 14. Orbital plots (right) of CO in the gas phase and upon interaction with the surface and (left) the corresponding O K-edge XAS and XES spectra.

due to overlap of mostly occupied orbitals. The 5σ is in the gas phase mostly on the carbon end due to a large contribution of C 2*s* but upon surface interaction it polarizes more towards the oxygen end to reduce the Pauli repulsion with the *d*-states; depending on the occupation of the *d*-shell the resulting contribution to the overall interaction may be attractive or repulsive [80]. The 5σ orbital is antibonding as evidenced, *e.g.*, by the shortening of the C—O bond upon ionization in gas phase [81]. The interaction with the substrate leads to a significant downward shift in the orbital energy as the antibonding character is relaxed. Also the 4σ (not shown in terms of orbital plots) is important and is mainly of O 2*s* character. The net bonding with the surface is then a result of the attractive π-interaction and repulsive σ-interaction that partly cancel each other. However, the interaction in each symmetry set of orbitals can be quite large even though the resultant bond is not very strong due to cancellation effects.

Based on this discussion we build the electronic spectrum we expect from the XES and XAS processes. Since we probe the states via the O 1*s* core orbital we project the electronic states on the oxygen atom. The occupied electronic states counted from high binding energy towards the Fermi level as seen from XES will then be 4 $\tilde{\sigma}$, 5 $\tilde{\sigma}$, 1 $\tilde{\pi}$ and $\tilde{d}_\pi$. An important effect of the 5σ orbital interaction is the different ordering with respect to 1π compared to the gas phase and the $\tilde{d}_\pi$ appears only through the surface bonding. Above the Fermi level probed by XAS, the 2 $\tilde{\pi}^*$ level is seen that has through internal polarization shifted down slightly. We can now address how these orbitals change upon laser excitation.

4.2. Transient observation of the precursor state

The desorption of CO from Ru(0001) has been well studied using femtosecond laser pulses as it provides an ideal system to probe the nature of bond breaking, a fundamental process in surface chemistry [15,82,83]. It is known that CO desorbs from a Ru surface after a single strong laser pulse with high enough fluence [13,15,83]. Based on two-pulse correlations with both 800 nm and 400 nm femtosecond lasers it has been shown that both hot electrons and phonons contribute to the desorption process [83] (see Fig. 5).

Fig. 15 shows the XAS and XES spectra of CO before and 12 ps after 400 nm laser excitation with 140 J/m^2 pulses [31,36]. There are clear shifts in the position and intensity of the O1*s* to 2 $\tilde{\pi}^*$ anti-bonding resonance of CO in the XAS spectra after laser excitation approaching the position of the free CO molecule. This indicates a significant weakening of the interaction with the surface after laser excitation. The intensity and position of the 2 $\tilde{\pi}^*$ varies with delay time and is shown in Fig. 16. We note that on short time scales (0–2 ps), the peak initially red-shifts and decreases in intensity, before moving towards the gas-phase peak, a topic that will be discussed in the next section. The 5 $\tilde{\sigma}$ and 1 $\tilde{\pi}$ CO orbitals are monitored in the XES spectra and after laser excitation show the same shift towards gas phase values as the 2 $\tilde{\pi}^*$ resonance. We can understand this since with a weaker interaction the strong 5 $\tilde{\sigma}$ peak will shift towards the Fermi level since the stabilization of the orbital decreases as discussed in the preceding section. This is further corroborated by the $\tilde{d}_\pi$ orbital, a non-bonding orbital which accompanies the formation of the CO to metal bond. On the same short timescale as for the 2 $\tilde{\pi}^*$ resonance, the intensity increases and then reverses after 1 ps and instead decreases to ~0.7 of its initial intensity after roughly 5–7 ps. This decreased intensity shows that the bond to the metal has been weakened, but CO is still interacting with the surface; the $\tilde{d}_\pi$ orbital only arises through this interaction. All these spectral changes are towards gas-phase CO and after 7 ps the spectra remain constant for the duration of the recorded timescale.

The question is if these spectra represent a combination of strongly chemisorbed CO and desorbed CO in the gas phase. In a detailed analysis using experimental chemisorbed and gas phase CO spectra to decompose the spectra measured at long time-delay it was found necessary to modify the resonantly excited XES gas phase spectra to account for differences in spectator shifts. These arise due to that in the resonantly excited XES measurements there is a localized electron in the 2π* orbital that will remain localized after the XES decay, causing shifts of the spectral lines as previously observed in the gas phase spectrum [84]. However, the spectator shift is smaller than in gas phase in the case of the long-time-delayed spectra shown in Fig. 15. In addition, the position of the 2 $\tilde{\pi}^*$ is not shifted fully to the gas phase value indicating that the weakened state is not gas phase but something else. It could be shown that this corresponds to CO molecules that are no longer chemically bonded to the surface, but in the thermally excited state still interact with the surface. This is easily seen in XAS since the spatial extent of the 2 $\tilde{\pi}^*$ wave function is much larger than the occupied orbitals making this state a sensitive indicator of surface interactions at longer distances. Fig. 17 shows the computed wave function of the excited 2 $\tilde{\pi}^*$ wave function at different distances from the surface and the corresponding shift in the 2 $\tilde{\pi}^*$ resonance. There is a clear overlap in the wave function as the CO center of mass to Ru distance has shifted from 2.6 Å to 4.5 Å. Thus, the observed evolution of the spectral features towards gas phase, but not quite reaching there even on longer (>12 ps) time scales, shows that there must exist a trapped state of CO further out from the surface on the path to desorption.

In order to explain the kinetics in adsorption and desorption processes on surfaces it has been necessary to include a weakly adsorbed transient species denoted 'precursor state' [64,85–87]. Here it was proposed that we indeed are observing such a weak transient precursor state. This was further inferred from DFT calculations of the potential of mean force of CO at various distances to the surface. Fig. 18 shows that for 0 K we observe the chemisorption well with the adsorption energy of 1.4 eV. Since the potential of mean force is normalized to the gas phase value adding temperature will result in an increase of the energy at the chemisorption well since the stiff perpendicular geometry of chemisorbed CO has much lower entropy than the freely rotating gas phase molecule. With increasing temperature the contribution of entropy increases further through the TΔS term. Since the DFT calculations were conducted with a functional that includes the van der Waals interaction the precursor state can be observed as a weak plateau further out from the surface. As the molecule is free to rotate, the entropy contribution is almost similar to the gas phase and there is not much change in the potential of

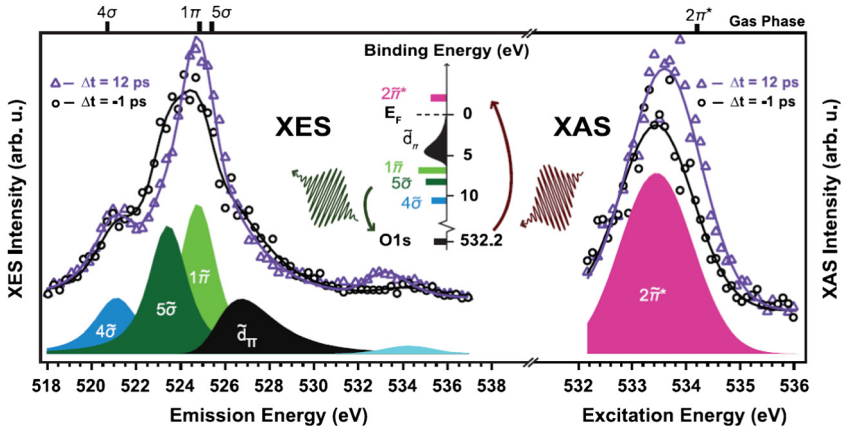

Fig. 15. Oxygen K-edge XES (left) and XAS (right) spectra (markers) of CO/Ru(0001) and corresponding fits (solid lines) measured at two selected pump–probe delays. Gas phase peak positions are shown on the upper scale. Reproduced with permission from Dell'Angela et al. [31].

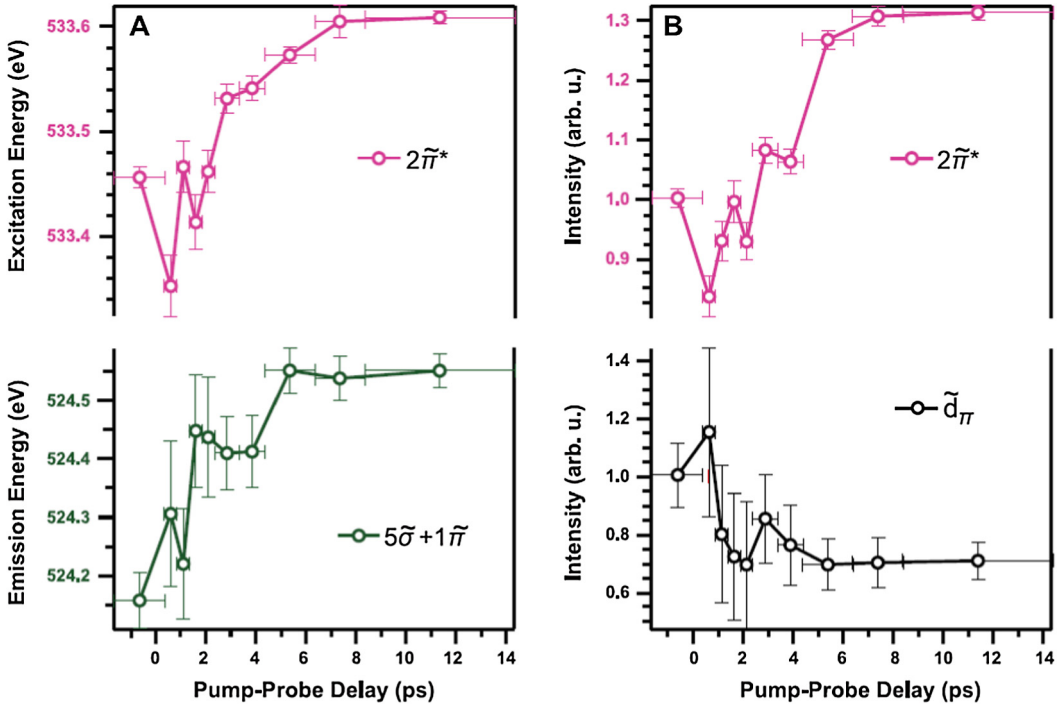

Fig. 16. The time evolution of CO electronic features in the X-ray absorption and emission spectra for CO/Ru(0001) after being excited by a femtosecond laser pulse. The $2\tilde{\pi}^*$ orbital increases in intensity and blue-shifts towards gas-phase CO values after the first couple of picoseconds. As these shifts occur in the CO $2\tilde{\pi}^*$ peak, the $\tilde{d}_\pi$ orbital decreases in intensity due to reduced interaction between the CO molecules and the ruthenium surface. These changes in the spectra indicate that the CO molecules are entering a precursor state prior to desorption/adsorption. Reproduced with permission from Dell'Angela et al. [31].

mean force when the temperature has reached 2000 K. At this temperature we observed indeed that the precursor state becomes isoenergetic with the chemisorbed state with an entropic barrier in between. Here we directly can see that molecules on the way to the gas phase can be trapped in the precursor state. The available average thermal energy, ~0.17 eV, at T = 2000 K is comparable to the well-depth in the precursor state (see Fig. 18) which means that molecules that leak through the entropy barrier can still be expected to be bound in the outer well. Once in the outer well, where they can reorient freely, there will be a high probability of becoming trapped there rather than re-entering the chemisorbed region. Since we observe the spectral intensity related to the precursor state on time scales up to 14 ps we assume that it exists for a quite long time. We anticipate that, after further collisions with the substrate, energy transfer occurs increasing or decreasing the kinetic energy and the molecules can either escape the trapped precursor state or return to the surface as it cools down.

These results are in agreement with sum-frequency generation (SFG) experiments [15]. In these experiments, the SFG intensity of the CO—Ru bond decreased by an order of magnitude, and recovered to half its original intensity after 170 ps as half of the CO molecules returned to their chemisorbed state. As SFG is a surface-sensitive technique, the initial loss of intensity was attributed to the CO molecules entering the same precursor state as observed here. As the CO molecules enter the precursor state, they

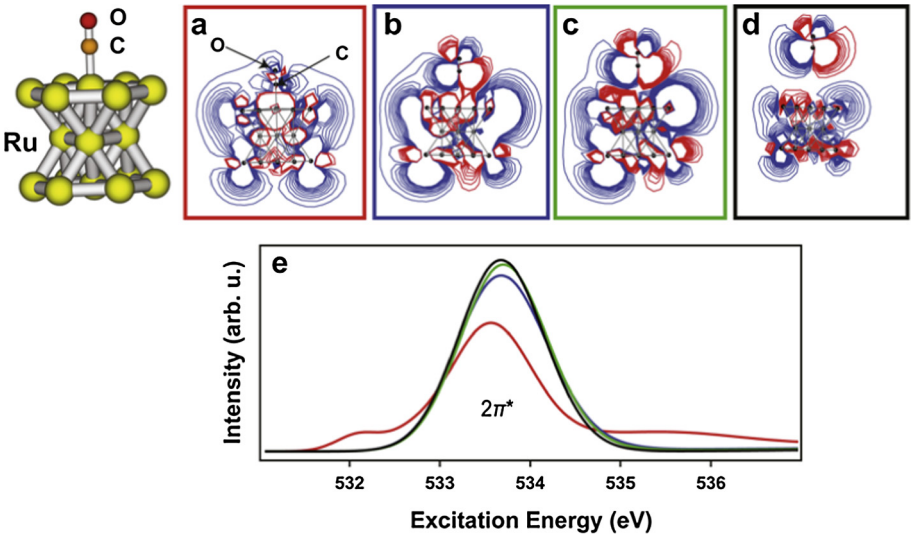

Fig. 17. **(a–d)** Iso-amplitude plots of wave functions of the core excited $2\pi^*$ amplitude calculated for CO on a 17-atom cluster model of the Ru(0001) surface sampling the potential energy surface from Figs. 35 and 37; blue indicates positive amplitude and red negative amplitude in the wave function. **(a)** Equilibrium structure for on-top CO. Center-of-mass (COM) distance 2.601 Å. **(b)** COM distance 4.0 Å (close to the inner turning point of the precursor well). **(c)** COM distance 4.5 Å (in the precursor well). **(d)** COM distance 6.75 Å (at the outer turning point of the precursor well). **(e)** Computed XAS spectra along the different points color-coded according to the frames in **(a–d)**.

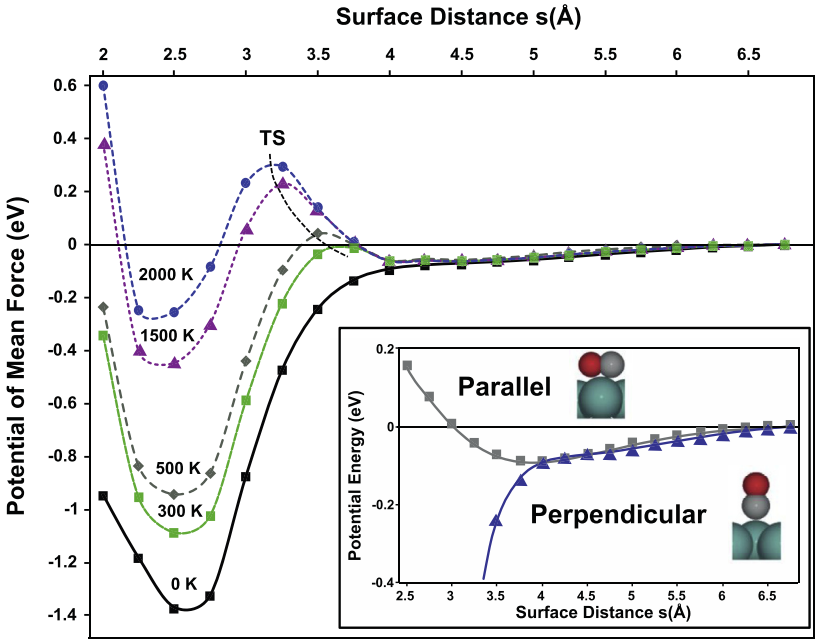

Fig. 18. The potential of mean force for CO adsorption/desorption on Ru(0001) at 0 K (minimum energy path, MEP) and 300, 500, 1500 and 2000 K. The inset shows the potential energy curve (0 K) of the CO molecule with orientation parallel and perpendicular to the Ru(0001) surface. The surface distance is measured between the CO center-of-mass and the surface. At 0 K and distances smaller than 2.5 Å CO moves from on-top to bridge and hollow sites giving less strong repulsion compared to the finite temperatures where more repulsive orientations are sampled. Reproduced with permission from Dell'Angela et al. [31].

interact less strongly with the surface, creating a decrease in the SFG intensity.

In the X-ray probe experiment, 30% of the $\tilde{d}_\pi$ orbital intensity had disappeared in the spectra by 7 ps after laser excitation. This decreased intensity is attributed to 30% of the CO molecules entering the precursor state. In the precursor state, the CO molecules can either desorb from the system or re-adsorb to the chemisorbed state as the surface cools. It was proposed from the SFG experiments [15] that 50% of the CO molecules in the precursor state re-adsorb to the surface, while the other 50% desorb. Indeed our AIMD simulations using a van der Waals function show exactly this type of trajectory with CO being trapped on the path to desorption in the precursor state and then readsorbing [32], as shown in Fig. 19.

CO desorption from Ru(0001) was also studied using X-ray spectroscopies at a lower optical laser fluence of 100 J/m^2 that generated quite different results compared to those at the higher 140 J/m^2 fluence [88]. The differences in the XAS and XES can be seen in Fig. 20. The most obvious change is the lack of evidence for the precursor state in the 2 $\tilde{\pi}^*$ resonance in the lower-fluence spectra. On short timescales (<2 ps), the behavior in the spectra between the lower and higher fluences is the same. We see an

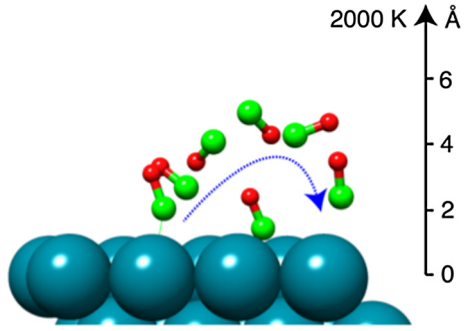

Fig. 19. Snapshots of CO desorption trajectories taken from AIMD simulations at 2000 K for CO/Ru(0001). Reproduced with permission from Xin et al. [32].

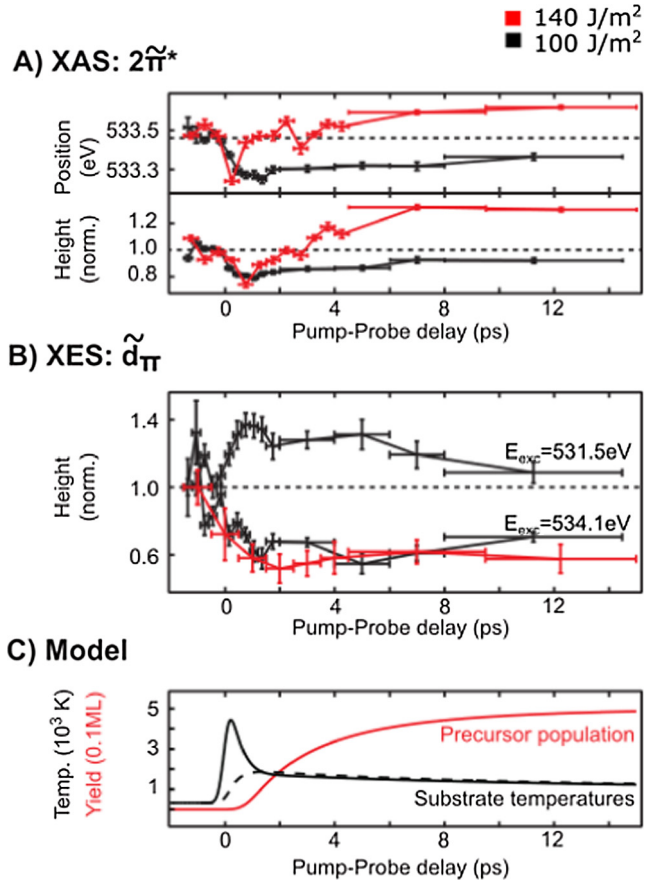

Fig. 20. Time evolution of the $2\tilde{\pi}^*$ resonance in XAS (A) and of the $1\tilde{d}_\pi$ -level (B) as a function of pump probe delay for 100 J/m^2 (black) and 140 J/m^2 (red) optical pump-laser fluences. In panel (B) the time-dependent spectra for 100 J/m^2 have been acquired at two excitation energies below and above the $2\tilde{\pi}^*$ resonance. On short timescales, both fluences show the CO molecules shift to higher coordination sites on the Ru(0001) surface. After 2 ps, the low and high fluence spectra separate as the CO molecules in the low-fluence spectra remain highly coordinated to the Ru (0001) surface while CO molecules in the high-fluence case enter the precursor state. Panel (C) shows the calculated time-evolution of the electron and phonon temperatures (black solid and dashed lines, respectively) together with the population of the precursor state (red line) obtained from an Arrhenius-like activation by the phonon temperature which transfers ~50% of the molecules into the precursor state (red). Reproduced with permission from Beye et al. [88].

increase in the $\tilde{d}_\pi$ intensity and shift to lower energy of the 2 $\tilde{\pi}^*$ which is related to CO moving along the surface but opposite to what has been described above for spectral changes related to the precursor state. From previous XAS and XES studies of CO molecules adsorbed in various sites [68,89,90] CO molecules move to more highly coordinated sites. After 2 ps, the 2 $\tilde{\pi}^*$ orbital in the lower-fluence spectra continues this trend, while in the high-fluence spectra the CO molecules reverse and become less coordinated to the surface as they enter the precursor state. The different behavior between the low and high fluences can be explained by looking at the electron-adsorbate, and phonon-adsorbate coupling. The frustrated rotation of CO is excited through electron-adsorbate coupling in both the low and high fluence regimes, leading to highly mobile CO molecules on the surface on timescales of <1 ps. The highly mobile CO molecules can occupy many sites on the surface, including bridge and hollow sites. As the phonon bath is heated up in the high fluence regime (>2 ps), the highly mobile CO molecules, through collisions with a heated and disordered substrate, enter the precursor state. In the low fluence regime, the phonon bath is not heated to sufficient temperatures to cause this transition.

We can now summarize the observations as to what occurs upon laser excitation of Ru(0001) with adsorbed CO, as shown in Fig. 21. During the first picosecond, hot electrons generated by the laser pulse lead to excitation of rotational and translational external vibrational modes resulting in motion parallel to the surface. This is detected through spectroscopic signatures indicative of partial population of CO in higher coordination sites. After a few picoseconds the additional impulsive excitation of the adsorbate by the substrate phonons initiates a fraction of molecules, in the present case around 30%, to move out from the surface and enter the precursor state. Here the molecules can rotate almost freely and thereby occupy a higher entropic state. The residence time in the precursor state is more than 25 ps and as the surface is cooled down around half of the molecules (in the present case) will reenter the chemisorbed state and the other half will leave the surface completely as desorbed molecules. This is an example of probing a transient state that will be almost impossible to observe under steady-state desorbing conditions in equilibrium with the gas phase since the population is extremely small. It is only by using ultrafast techniques that it becomes possible to observe such a short-lived state and then only by increasing the population by several orders of magnitude under extremely short times.

4.3. Co-adsorbate effects on desorption

In the pump-probe experiment described above, the desorption of CO from Ru(0001) showed a significant blueshift of the CO $2\pi^*$ peak towards the gas phase (see Fig. 22(a)). This increase in intensity is consistent with a desorption pathway mediated by a weakly bound precursor species, a state that has long been hypothesized based on kinetic measurements [64,65,87,91,92]. Under relevant reaction conditions the catalyst surface will contain many different adsorbates and, depending on type, coverage and orientation of the catalyst surface, these species can cause significant changes in the surrounding surface electronic structure and hence the measured desorption dynamics. In a recent study, we found that co-adsorbed oxygen atoms have a considerable influence on the desorption mechanism of CO from the Ru(0001) surface [32]. In Fig. 22(a), the measured O *K*-edge XAS spectra are shown for the CO/Ru(0001) and CO + O/Ru(0001) cases. The distribution of unoccupied CO 2 $\tilde{\pi}^*$ states clearly shows that the optical laser pump has a larger effect on the CO/Ru(0001) system than on the CO + O/Ru(0001) system and that the observations are indicative of the disappearance of the CO precursor state in the latter system. To fully interpret this effect we need to first understand how the laser affects the electronic states of the surface-adsorbate system.

When a femto-second laser pulse excites the substrate electron distribution, a large carrier density and hence a significant number of electronic energy transfer processes (excitation and de-

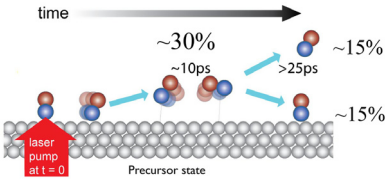

Fig. 21. Schematic illustration of the dynamics of CO adsorbed on Ru after optical laser excitation.

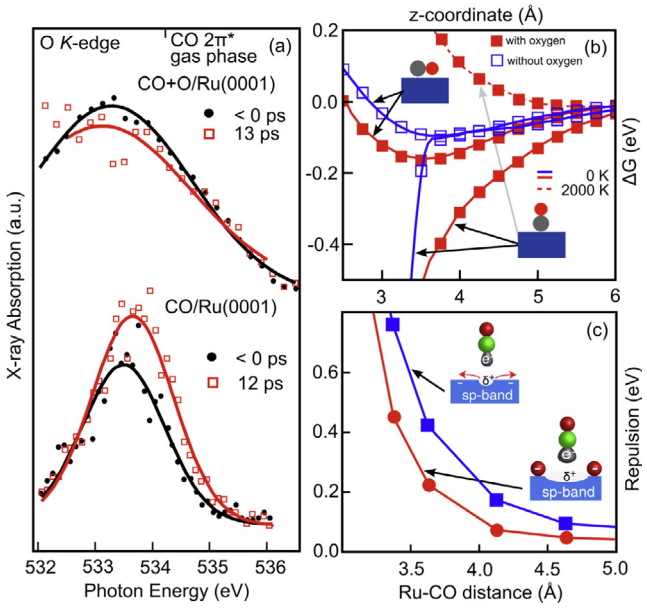

Fig. 22. (**a**) O K-edge spectra showing the CO $2\tilde{\pi}^*$ states on CO/Ru(0001) and CO/O/Ru(0001) as measured before and >10 ps after the laser pump. (Note that the peak for atomic oxygen is well separated from the CO peak as shown in Fig. 13) (**b**) Free-energy profiles of CO desorption with (red) and without (blue) co-adsorbed oxygen along parallel and perpendicular constrained pathways. Solid lines are at 0 K and dashed line at 2000 K. (**c**) Calculated repulsive interaction energies between CO and Ru(0001) with (red) and without (blue) co-adsorbed oxygen. Energies are obtained from frozen-orbital calculations. Insets in (**c**) show CO 5σ interaction with the Ru sp-band with and without co-adsorbed oxygen. Reproduced with permission from Xin et al. [32].

excitation) can be achieved. Electrons excited into adsorbate-surface antibonding states will deposit energy into the surface-adsorbate bond thus leaving the system in a vibrationally excited state. If the relaxation time of the vibration is longer than the time needed to re-excite the resonance then sufficient energy can be deposited into the surface-adsorbate bond to induce desorption. The soft vibrational modes of CO on the surface of Ru(0001), indicated by DFT calculations, is the predominant reason for the existence of a weakly bound precursor state. When oxygen is co-adsorbed on the Ru(0001) surface our femto-second time-resolved measurements show that the signature for the weakly bound CO precursor state disappears as seen in Fig. 22(a), thus indicating that the CO desorption occurs entirely through a direct pathway. To elucidate this difference we needed to compute the free energy of CO desorption along well defined pathways on the clean and oxygen-covered Ru(0001) surface. As described in the Methods section, free energies along the reaction coordinate were calculated using DFT and applying a potential of mean force approach in which all possible degrees of freedom perpendicular to the reaction coordinate were taken into account [64,65]. In Fig. 22(b) we see the free-energy paths of CO desorbing from the surface with and without oxygen in a parallel or perpendicular orientation relative to the surface. The precursor state of CO on clean Ru(0001) can be seen as a consequence of the coinciding energy of both CO orientations at longer distances, where the molecule is still bound to the substrate. This clearly suggests that CO has significant degrees of freedom in the precursor region resulting in an entropy-induced shallow adsorption minimum at higher temperatures, which is separated from the chemisorbed state by an entropic barrier.

In the case where atomic oxygen is present on the surface the CO desorption energetics profile in Fig. 22(b) evidently shows that desorption when CO is perpendicular to the surface is favored. In contrast to the clean surface this leads to a constrained desorption pathway and therefore a lack of entropic stabilization in the region where a precursor state would be expected. Hence, at higher temperatures, if CO on the oxygen-covered Ru(0001) surface crosses the barrier for desorption, it will proceed directly into the gas phase as shown by the dashed line in Fig. 22(b).

The free-energy profiles in Fig. 22(b) display a significant stabilization of CO in the precursor region on the surface with co-adsorbed oxygen compared to the clean surface. This increase in stability is the predominant reason why the precursor state vanishes in the system with co-adsorbed oxygen. To understand what drives this, one has to look at changes in the electronic structure in the relevant region. The insets in Fig. 22(c) show schematically what the difference is between the two systems. The oxygen in the vicinity of the desorption site withdraws electron density from the site making it positively charged. This effectively leads to less σ-repulsion which also results in a stronger electrostatic attraction between CO 5σ and the now positively charged site. A way to quantify this is to look only at the orbital orthogonalization in the near precursor region. In Fig. 22(c) the repulsive energy as a function of the Ru—CO distance is calculated using a frozen orbital approach [66]. The calculations show that there is an oxygen-induced reduction in the orbital overlap corresponding to a decrease in Pauli repulsion. This, together with an increase in electrostatic attraction, is what causes the CO desorption along the direct pathway in the case of CO/O/Ru(0001) instead of the precursor-mediated pathway found for CO/Ru(0001).

To further elucidate the mechanism we performed AIMD simulations of the process on Ru surfaces that had no co-adsorbed oxygen and where there was a 2:1 oxygen to CO ratio. The simulations were run at a temperature of 2000 K and, based on the free-energy profiles of desorption, this temperature should be sufficient to overcome the entropic barrier to desorption and hence provide mechanistic insight into the process on the two surfaces. What we found from the simulations was that CO desorption on the bare Ru surface occurred on a much longer timescale than on the surface with co-adsorbed oxygen. These observations are consistent with the existence of a weakly bound precursor state in which there is strong coupling to soft rotational modes of CO. On the oxygen-covered surface the coupling to the rotational modes is very weak leading to increased momentum in the direction away from the surface and hence a much shorter timescale for desorption. The combination of experimental and theoretical efforts has clearly provided a mechanistic understanding of surface chemical bonding and the dynamics of desorption under varying surface conditions.

5. Atomic O on Ru(0001)

Recent experiments indicate that laser excitation of electrons in the metal surface directly into the unoccupied adsorbate orbitals may play an important role. Two-photon photoemission (2PP) spectroscopy studies of adsorbates on noble metals have shown little evidence for a hot electron mechanism, while some studies

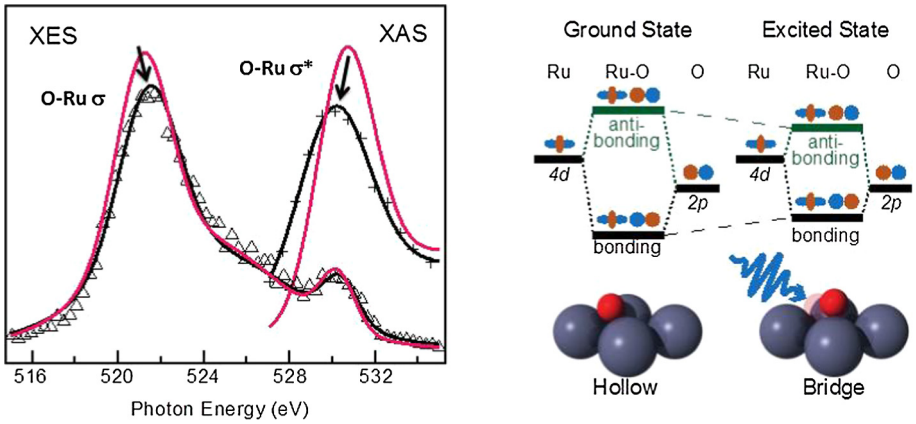

Fig. 23. (Left) XES and XAS spectra of atomic oxygen on Ru(0001) showing the bonding (XES) and antibonding (XAS) states. The spectra with markers and full black line are obtained after the optical laser pump and integrated over the interval 0.1–4 ps. Compared to the reference spectra (full red line) before the laser pump the bond weakening is directly evidenced through the reduced split between bonding and antibonding states in the measured spectra. **(Right)** Schematic illustration of the process leading to the spectra on the left. The chemisorption of oxygen on Ru(0001) leads to formation of bonding and antibonding states involving O 2p and Ru 4d with a split which depends on the strength of the interaction. The split is then reduced when oxygen is activated and comes up from the hollow towards bridge. Reproduced with permission from Beye et al. [33].

have shown strong evidence for direct absorption [93,94]. In other experiments, the results of CO oxidation on Ru(0001) and Pt(111) could only be explained through a mixture of hot electrons and a linear, non-thermal absorption process [12,95]. The reaction yield for the non-thermal mechanism scaled linearly with laser fluence, indicating that the process was a single-photon process. A strong candidate to explain this process is then the direct excitation of an electron from the metal surface to the O—Ru anti-bonding orbital [3,36].

5.1. Bonding and antibonding orbitals and bond-activation

Forming a covalent bond between two atoms results in new molecular orbitals where the bonding state is stabilized while the antibonding is destabilized relative to the original states (see schematic illustration in Fig. 23); the bonding state is the in-phase combination leading to build-up of charge density between the nuclei while the antibonding changes phase, giving a node plane and charge depletion between them. In the case of atomic oxygen on Ruthenium the bond-formation as illustrated is between the O 2*p* and Ru $4d_\sigma$ which points in the direction orthogonal to the surface plane. The equilibrium geometry is with the oxygen atom in a hollow position with a significant split (~9.6 eV) between the bonding (measured in XES) and antibonding (measured in XAS) states. The femtosecond pulse from the optical laser activates the oxygen atom by transiently populating the antibonding state with electrons excited from the metal, which weakens the bond, and also by heating the metal and adsorbate as the hot electron distribution equilibrates with the vibrations of the metal and adsorbate. The result is large-amplitude vibrations of the oxygen atom which comes out of the hollow position and moves towards bridge where it interacts more weakly with the metal since there it interacts with fewer metal atoms. This is seen directly in the spectra where now the XES peak from the O—Ru σ bond has shifted to higher energy while the antibonding O—Ru σ* peak in XAS has shifted towards the Fermi level, *i.e.* to lower energy; the measured split is now reduced to ~8.6 eV.

The spectra shown here illustrate the formation of both bonding and antibonding states when a covalent bond is formed; this is a well-known concept in molecular orbital theory. The changes seen here upon activation of the oxygen are as expected, but had never before been measured directly in the electronic structure. Two prerequisites made this possible: the X-ray spectroscopies for measuring the electronic structure and the time-resolution provided by the XFEL to enable measuring the transient changes in the electronic structure. We will in the next section give more details on these measurements.

5.2. Optical laser-induced activation of atomic oxygen

In Fig. 24, we display schematically the electronic structure of atomic oxygen adsorbed on a ruthenium surface together with XAS and XES data for the ground state of the system. As discussed in the preceding section upon chemisorption of oxygen on ruthenium, the atomic oxygen valence 2*p* orbitals mix with the Ru 4*d* band and split up into two energetically distinct sets of hybrid orbitals – the bonding orbitals (occupied, studied with XES, grey) and the antibonding orbitals (mainly unoccupied, studied with XAS, green).

In contrast to many other systems, atomic oxygen chemisorbed on a ruthenium surface is rather strongly bound and does not desorb upon laser excitation. Thus, the dynamics of the system cannot be studied with a mass spectrometer but have to be analyzed with an XFEL directly in the electronic structure. On the other hand, experimentally, since oxygen does not desorb, the experiment is non-destructive: the surface restores to the initial state upon cooling down after the laser excitation and does not require reduced excitation repetition rates and rapid scanning of the sample.

Upon excitation with an ultrashort optical laser pulse, the bond of atomic oxygen to the ruthenium surface is weakened. From our data, we can conclude that this bond weakening, and thus the activation of oxygen for surface reactions, occurs before the phonon system of the substrate heats up. Therefore, oxygen is enabled to react before possible reaction partners desorb through coupling to the hot phonon bath in the substrate. This opens an ultrashort window of time with non-equilibrium between the electron and phonon heat baths in the substrate during which reactions can evolve, also under the present ultra-high vacuum (UHV) conditions.

For the shown XES spectrum, the excitation energy range between 529.2 and 530.4 eV was selected. Summing the entire recorded emission signal in the range between 517 and 537 eV yielded the XAS spectra. Relative intensities between the shown XES and XAS spectra are arbitrary. The sample, a $p(2 \times 1)$ layer of

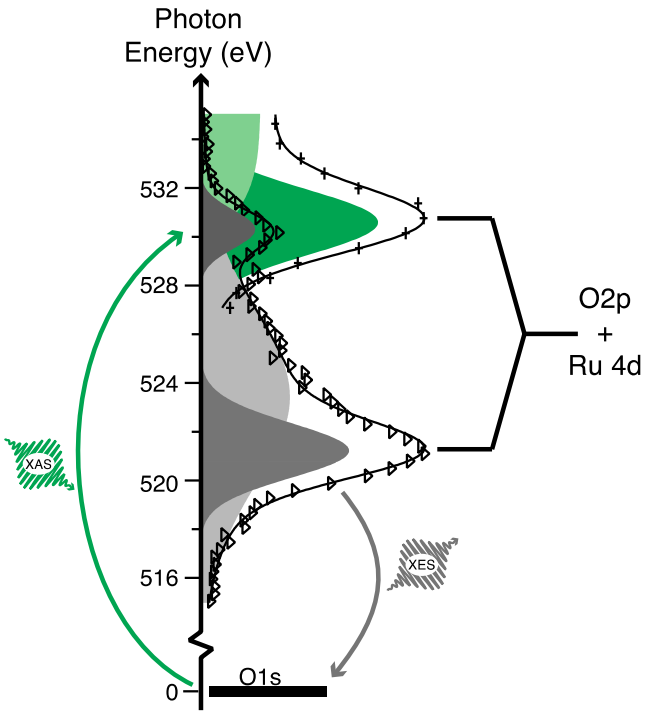

Fig. 24. The electronic structure of oxygen adsorbed on Ruthenium is studied with absorption and emission spectroscopy. Two main features are observed as a result of the intermixing of Oxygen 2*p* valence states with Ru 4*d* metal band. The features can be separated into unoccupied antibonding states (green, apparent in XAS) and mainly occupied bonding states (grey, apparent in XES). Experimental data are shown as symbols, filled areas display the different components for the line fit shown as a solid line. Reproduced with permission from Beye et al. [33].

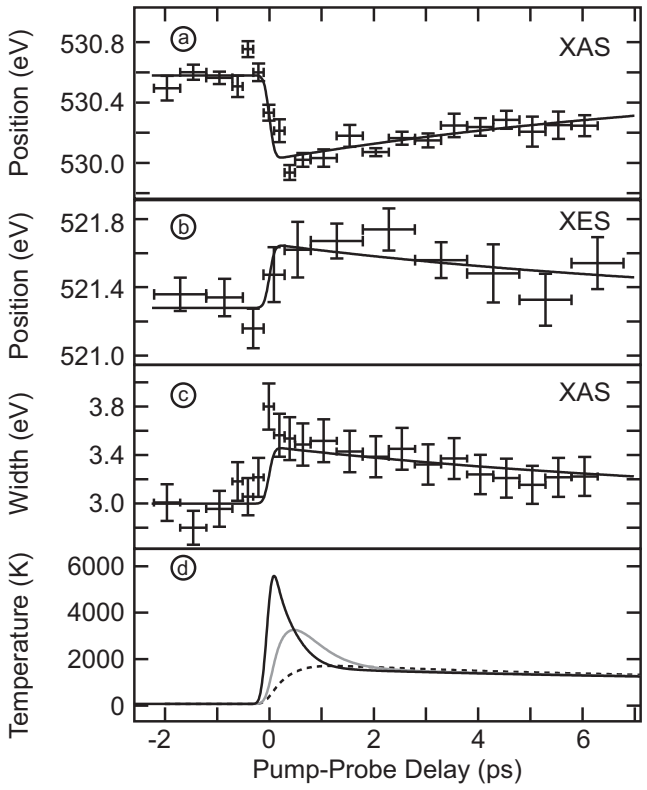

Fig. 25. Panels **a–c** display the time evolution of the fit parameters together with a global fit of the underlying time constants. The initial changes are limited by the time resolution while the system cools down on a 5–10 ps time scale. Panel **d** shows a three-temperature model calculation for the metal electrons (solid black), the metal phonons (dashed black) and the atomic oxygen adsorbate temperature (solid grey) as obtained applying an *ab initio* electronic friction parameter. Reproduced with permission from Beye et al. [33].

oxygen prepared on a Ru(0001) surface, was scanned during the measurement only as a precaution. The soft X-ray beam energy was scanned around the O K-edge with the monochromator resolution set to 250 meV and derived from an 80 fs electron beam. The optical laser was *p*-polarized to the sample surface and set to a fluence of about 140 J/m^2. Temporal jitter between both pulses was measured and corrected for, but the optical laser pulse length of about 170 fs limited the time resolution to around 190 fs. Fig. 24 also shows how we analyze the different contributions to the spectra using curve fitting: the XAS spectra are separated into a Gaussian representing the antibonding oxygen orbitals and a hyperbolic tangent function modeling the continuum edge jump. The XES spectra contain contributions from rather sharp oxygen-derived bonding states (Gaussian at 521 eV) and a broad feature with mainly Ru 4*d* character (Gaussian around 531 eV). It is assumed that the latter is fixed in position, height and width relative to the main peak. The XES spectra also show a feature related to elastic scattering of the incoming light (and thus moving with the excitation energy). This peak provides the energy calibration of the spectrometer and is also modeled with a Gaussian.

For each pump-probe delay we perform the described fits and obtain the characteristic time traces as shown in Fig. 25. The XAS peak shifts to lower energies by about (-0.56 ± 0.07) eV, while the XES peak shifts to higher energies by (0.37 ± 0.11) eV, thus the splitting between the bonding and the antibonding states is reduced. The increase in the width of the XAS spectrum is accompanied by a decrease in peak intensity, such that the area stays constant and thus the number of unoccupied O 2*p* states is constant [19]. A similar change is observed in the XES but with less statistical significance. The lines in Fig. 25 result from a global fit to the displayed data, but should mostly be considered as a guide to the eye. Within our time resolution of 190 fs, an immediate change of the parameters is observed, after which relaxation back to their original values occurs on a timescale of 5–10 ps.

To elucidate the reaction pathway, we performed three-temperature model calculations (Fig. 25), using the substrate electron and phonon baths coupled with standard parameters and a coupling of the oxygen vibrations to the metal electrons as anticipated from the ultrashort excitation time scale. The coupling of the oxygen atom to the hot electrons is calculated as an *ab initio* electronic friction from an electron-phonon coupling calculation with QUANTUM ESPRESSO where we obtain 0.5 ps^{-1} for lateral motion and 2.5 ps^{-1} for perpendicular motion. The temperature evolution of the adsorbate is evaluated with this coupling parameter and reaches the maximum at 500 fs, instead of the observed 190 fs limited only by the temporal resolution. This hints to a non-thermal mechanism of oxygen activation in agreement with the work by Bonn et al. [13] and also with our studies using 800 and 400 nm light and two-pulse correlations together with theoretical DFT simulations [12].

We suggest that the missing, fast contribution comes from the initial, non-thermal electron excitations mainly into the antibonding O—Ru states (see Fig. 26). This occupation weakens the chemisorption bond and drives the oxygen atoms away from the strongly bound hollow site. This bond weakening reduces the splitting between the bonding and anti-bonding orbitals, which becomes evident through the observed shift of the XAS and XES features. The proposed non-adiabatic coupling of adsorbate motion and the electronic system could explain the initial changes in the

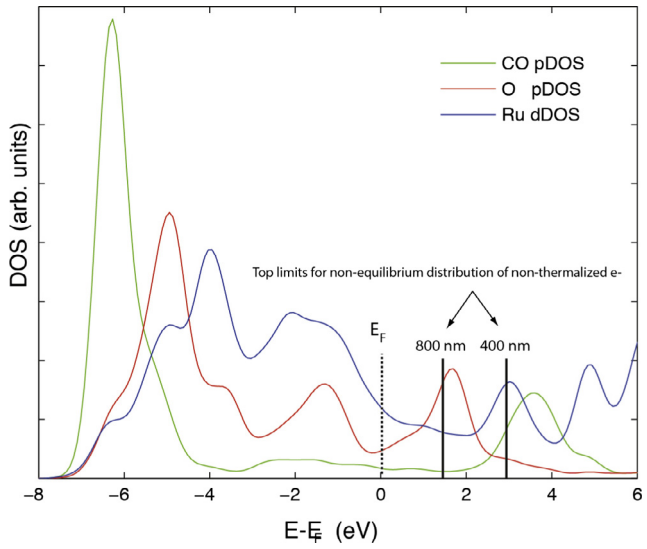

Fig. 26. Computed density of states for the coadsorption system CO/O/Ru(0001) with the maximum position relative the Fermi-level (E_F) of excitations using 400 and 800 nm light indicated. Since most excitations will involve electrons from below E_F the 400 nm laser will be more efficient in exciting electrons into the O—Ru antibonding σ^* states around 1.8 eV. Reproduced with permission from Öberg et al. [12].

adsorbate electronic structure that proceed faster than anticipated from the electronic friction model. Next we will connect the results for CO desorption and activation of atomic oxygen to the model reaction of CO oxidation using atomic oxygen chemisorbed on Ru (0001).

6. CO oxidation

With the different components such as CO, O and also desorption of CO in the presence of co-adsorbed O we can now increase the complexity and look into a full surface chemical reaction and observe bond formation in real time. Here we will address the potential to observe the transition state region as the reactants are coming together under ultrafast timescales.

6.1. Optical laser-induced CO oxidation

Under UHV conditions, CO and O co-adsorbed on Ru(0001) do not spontaneously produce carbon dioxide (CO_2) under thermal heating. This is because the thermal desorption temperature of CO is lower than the thermal CO oxidation temperature, leading to desorption of all CO before CO oxidation is thermally favored. The reaction can, however, be initiated using femtosecond laser pulses, which create high surface temperatures on short timescales. The temperatures are needed for CO oxidation in order to activate the surface O species, this is often thought to be the limiting step in CO oxidation due to the high binding energy of O to Ru (0001) (~6 eV). CO is still the primary laser-induced desorption product, as only ~3% (800 nm light) or ~10% (400 nm light) of the CO molecules leave the surface as CO_2, depending on laser fluence, and no O_2 is formed [12,13]. There is therefore a competition between the thermodynamics of CO desorption and the kinetics of CO oxidation.

Here we will describe ultrafast studies of the CO + O reaction on Ru(0001) using XAS and XES. The reaction was initiated using pulses from a 400 nm optical laser. Changes in the occupied and unoccupied electronic structure during reaction conditions were monitored using ultrafast soft X-ray absorption spectroscopy and X-ray emission spectroscopy. Time-resolved electronic structure maps for oxygen were obtained selectively from the electronic states projected onto either the adsorbed atoms or the oxygen in the CO molecules using the energy selectivity in XAS. Fig. 27(A) shows the O K-edge XAS spectra for negative time delays and at 1.5–3.0 ps after laser excitation, while Fig. 27(B) shows the time evolution of the important spectral features from part (A).

The rapid response evidenced in the shoulder between 528 and 529 eV corresponds to the activation of the O species on the surface. The increased intensity appears on a timescale of 280 ± 100 fs, which is faster than the time resolution of the experiment. The O species couple strongly to the electron bath, where an electron from the surface transfers transiently to the O—Ru antibonding orbital as described above, weakening the bond and increasing the bond length. The occupation of the anti-bonding orbital is short-lived, and the O—Ru bond strength increases again, though the O—Ru bond distance is now elongated from the equilibrium. This increased bond distance manifests itself as kinetic energy in form of nuclear motions of the O surface atoms as the

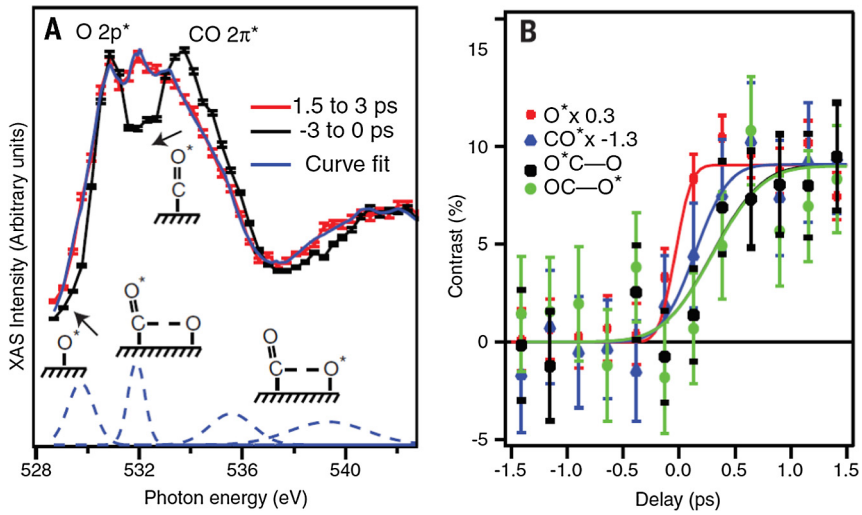

Fig. 27. Measured X-ray absorption spectra with time-dependent changes. (A) Pump-probe O K-edge XAS spectrum of CO/O/Ru(0001). (B) Time development of the spectral intensities in four different spectral regions plotted as the contrast. Reproduced with permission from Öström et al. [3].

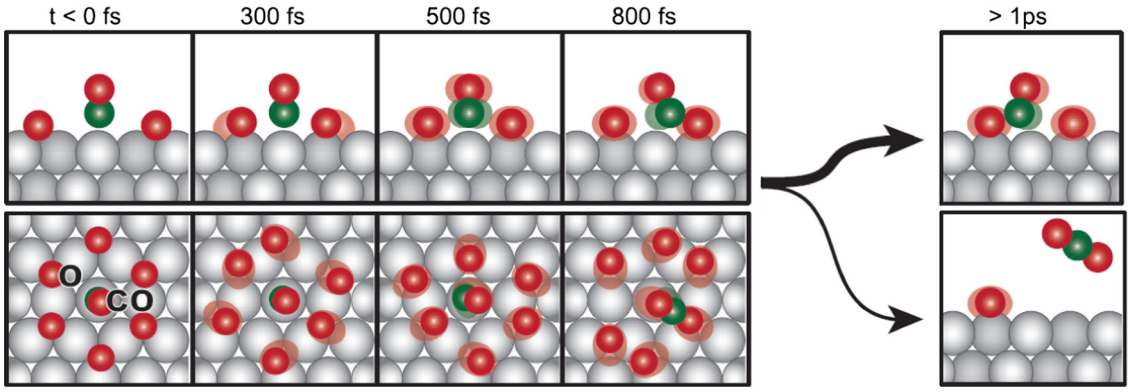

Fig. 28. Schematic of the different steps in the laser-induced CO oxidation on Ru(0001), including relevant timescales. Reproduced with permission from Öström et al. [3].

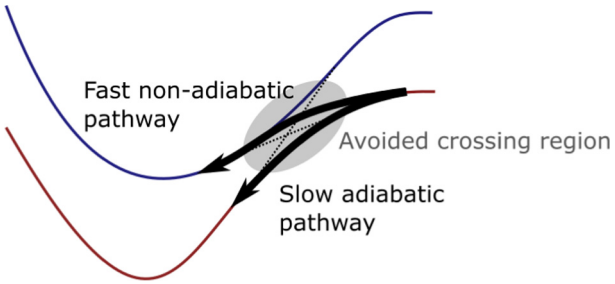

Fig. 29. A diagram showing the difference between adiabatic and non-adiabatic processes.

transiently excited electron delocalizes back into the conduction band. The O atoms, which normally reside in the hollow site on Ru(0001) gain enough kinetic energy in this process to move to less coordinated sites, such as bridge sites, leading to a shift towards lower energy in the XAS spectra. These activated O atoms can more readily interact with the surface CO species. From the experiment it cannot be distinguished if the occupation of the O—Ru anti-bonding orbital is a result of high-energy surface electrons transferring to the orbital, or if the electrons are directly excited from the metal to the anti-bonding orbital.

The CO molecules on the surface are also activated, though at slightly longer timescales of 550 ± 120 fs. This can be seen in the red-shift of the CO 2 $\tilde{\pi}^*$ peak. The activation of the CO molecules corresponds to excitation of the frustrated rotation of CO, a mode that is also excited through efficient electron coupling. The frustrated rotation increases the translational motion of CO on the surface, and the CO molecules can move to more highly coordinated sites, such as bridge and/or hollow sites.

The increased mobility of both surface species leads to increased interaction between CO and O and attempts to react, which in a minority of instances results in the formation of CO_2. These attempts to form the new bond between CO and O can be seen around 800 ± 250 fs, where new states related to this interaction appear in the region between 536 eV and 539 eV, and around 532 eV. This process is schematically shown in Fig. 28.

6.2. Non-adiabatic effects

When modeling chemical reactions, the electron-nuclear motion degrees of freedom are typically decoupled from each other using the Born-Oppenheimer approximation in order to lighten computational costs. In the Born-Oppenheimer approximation, the wave function of the system is written as:

$$\Psi = \psi_{Electronic} \cdot \psi_{Nuclear}$$

where $\Psi_{Electronic}$ is the wave function for the electrons, and $\Psi_{Nuclear}$ is the wave function for the nuclei. Separating these terms creates a separation between the nuclear and electron degrees of freedom, leading to the calculation of adiabatic potential energy surfaces. This assumes that the first and second derivatives of the electronic wave function with respect to nuclear displacements can be neglected, and that, from the perspective of the electrons, the nuclei are thus frozen in time. When this approximation is applicable it thus corresponds to the electrons always adiabatically adjusting to the lowest energy configuration, forming adiabatic potential energy surfaces in which the kinetic energy of the nuclei is ignored. Reactions are then assumed to proceed down these adiabatic potential energy surfaces and the total energy for the system can then be written as the sum of the energy for the electrons and the energy for the nuclei:

$$E_{Total} = E_{Electronic} + E_{Nuclear}$$

The separation of electronic energy from nuclear energy prevents the system from jumping between adiabatic potential energy surfaces. Due to these constraints, two adiabatic potential energy surfaces cannot cross, resulting in an avoided crossing. On metal catalysts the energy spacing between electronic levels is quite small due to the large number of states that are involved. During a chemical reaction, as the system evolves from reactants to products, the electronic structure is constantly changing. It is therefore likely that the system can jump between ground-state and low-lying excited state potential energy surfaces during reaction conditions, which causes a breakdown of the Born-Oppenheimer approximation. This would constitute a non-adiabatic effect and is illustrated in Fig. 29.

The importance of non-adiabatic effects on surface reactions depends heavily on the reaction that is considered. For example, Bungaro et al. [96] successfully modeled the dynamics of oxidation of Mg(0001) by O_2 using an adiabatic theory. In agreement with experiments, they found that oxygen is adsorbed below the Mg surface, forming ionic islands commensurate with the metal lattice [97]. Adiabatic theories, however, predict millisecond vibrational lifetimes for the CO($v = 1$) vibrational relaxation on a Cu surface due to the phonon-vibrational energy mismatch. However, the experimental lifetime was found to be on a picosecond timescale, which was correctly modeled only by including the nonadiabatic process of electronic friction [98,99]. Modeling nonadiabatic processes is extremely difficult and it is important to compare these theoretical models with experimental evidence.

One such system in which nonadiabatic effects are important is CO oxidation on Ru(0001) [12,13]. The limiting factor for CO oxi-

dation on Ru(0001) has often been considered to be the strong bond between the atomic oxygen and the surface. Upon laser excitation, high-energy electrons can occupy the O—Ru anti-bonding orbital that lies about 1.8 eV above the Fermi level (see Fig. 26). Occupation of this orbital weakens the O—Ru bond, leading to a lengthening of the bond and promoting the O atom into a vibrationally excited state. Vibrationally excited O atoms are mobile on the surface, leading to more interactions with the CO molecules and attempts to form CO_2. The conversion between electronic and vibrational energy of the oxygen atoms plays an integral role in the formation of CO_2 and constitutes to some extent a breakdown of the Born-Oppenheimer approximation as it is a strongly non-adiabatic effect. It is critical to study systems, such as CO oxidation, in which both adiabatic and non-adiabatic effects play important roles, in order to fully understand chemical reactions at catalytic interfaces. The ability to accurately model reactions depends on understanding the interplay between ground-state, adiabatic processes, and excited-state, non-adiabatic processes.

6.3. Transition state

In chemistry, the concept of the transition state is useful to describe the reaction dynamics. The transition state is a highly unstable species with an energy barrier as the reactants move towards products, as shown in Fig. 31. The state is unstable due to the unfavorable geometric configurations the specie must pass through as it transitions from one state to another. Because of the instability of the transition state, it was thought to have a very short lifetime, making it difficult to observe experimentally. The main challenge lies in the typically very low conversion rate at a given site under steady-state conditions; this can be overcome by initiating the reaction with an optical femtosecond laser which results in a more concerted approach to the transition state. A probe with high temporal resolution is furthermore needed to directly observe these states.

As the CO oxidation is initiated, the O and CO species begin to interact. In Fig. 27, the evidence for the CO and O species near and/or at the transition state can be observed. The species must overcome an energy barrier to form CO_2. Fig. 28 illustrates the reaction where CO is bound on-top and surrounded by six oxygen atoms in a honeycomb structure. As the system is activated by the optical laser pulse, the oxygen atoms and CO begin to move along the surface and encounter each other and attempt to form the new bond. Most attempts fail, as evidenced by the low yield of CO_2, and the CO rebounds and will collide with another oxygen atom at the surface. The molecules will make many attempts to overcome the energy barrier, creating a distribution of states along the reaction coordinate. Temperature is the driving force providing the energy needed to overcome the transition state barrier, so the probability of being in the transition state region is strongly dependent on temperature; the higher the temperature, the higher the probability of finding the system near the transition state, but how much time is spent in the transition state region?

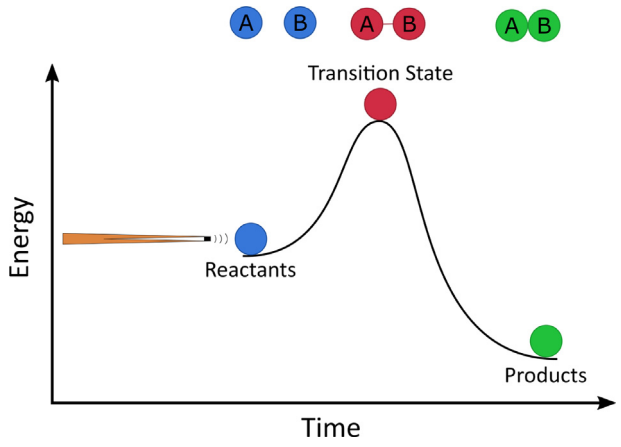

Fig. 30. The transition state contains an energy barrier between reactants and products. The slowing down at the transition state is illustrated here using a classical analogy of shooting a billiard ball over a small hill.

We would normally conclude that these states would be too short-lived to be observed in the spectra. The observation of the molecules near the transition state in Fig. 27 can be rationalized through classical potential energy barriers (Fig. 30). At the top of the barrier, the maximum amount of kinetic energy has been converted into potential energy. This slows down the reaction dynamics, allowing states near the transition state to become long-lived, and hence accessible if the concentration is large enough. Quantum mechanically, this is also true, as we have an enhanced probability at the classical turning points for a highly excited vibrational motion. Fig. 31 illustrates the process where the CO caged by the oxygen atoms is modeled through a harmonic oscillator potential. It is clear that, particularly for the more highly excited levels, the probability of finding the system near the classical turning points is strongly enhanced; the probability of being in that region is shown as a function of temperature in the right side of Fig. 31. Once the transition state barrier has been overcome, the potential energy will be converted back to kinetic energy, and the species will readily produce CO_2. These results are among the first direct observations of the occupation of states near the transition state region, highlighting key aspects of transition state theory, and the role it plays in chemical reactivity and kinetics.

6.4. THz-induced CO oxidation

Controlling reactions at surfaces has long been a goal of the surface science community. Reactions at metal surfaces are often initiated using femtosecond optical lasers. In this process, the electron bath of the system absorbs the energy, creating a high-energy electron distribution. Over a few picoseconds, the electron bath decays into the phonon bath, heating it up in the process. Either the electron bath or the phonon bath can couple to reactants and initiate a chemical reaction. It is, however, not currently possible to control the direction of energy flow in this process, leading to little control in selecting desired products. Ultrafast, intense terahertz (THz) sources provide an interesting opportunity at metal surfaces to steer the reaction down a specific reaction channel. Intense, ultrashort THz pulses have an associated large electric field vector. The electric field strength and orientation can be tuned for optimal interaction with charged and polar molecules. This has been shown in the gas phase where intense, single-cycle THz pulses were used to induce field-free orientation and alignment of OCS molecules [100].

On metal surfaces, the use of strong electric fields shows much promise due to the interaction of the THz pulse with the electron bath of the system. Due to dielectric screening, the electric field component of the THz pulse won't penetrate into the metal, however, on the surface boundary, the THz pulse can strongly interact with adsorbed molecules [101] or the electron bath [102,103]. The electric field intensity at metal surfaces can even be further enhanced by protrusions on the surface [102].

The electric fields of THz pulses can be separated into component electric field vectors that are either perpendicular or parallel to the surface. The electric field vectors perpendicular to the surface shift electron density either towards or away from the surface atoms, depending on the sign, before being screened out by the induced polarization in the metal. This change in electron density can partially empty or fill bonding orbitals in the chemical bonds

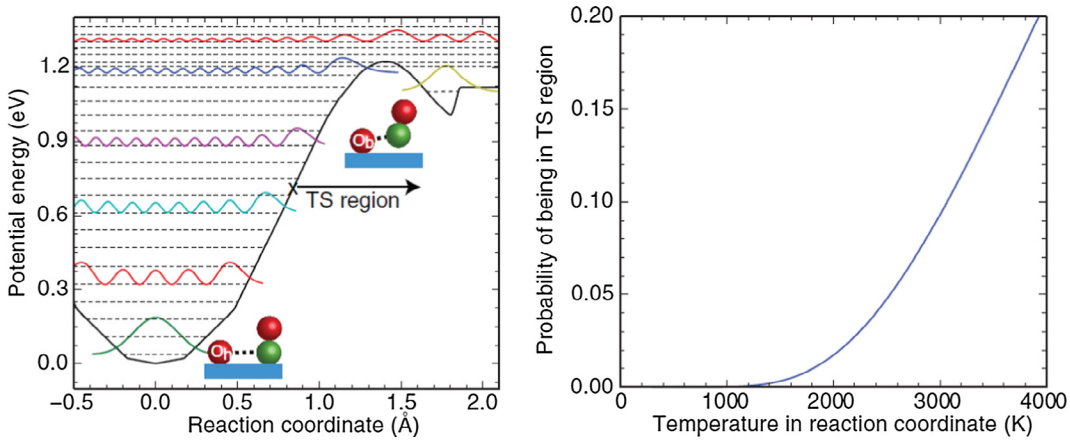

Fig. 31. (**Left**) One-dimensional harmonic oscillator model of CO caged by the oxygen atoms where it will move back and forth encountering first one oxygen and then bouncing over towards the other. The figure shows the energy levels and selected vibrational wave functions. For more highly excited vibrations the probability of being near the classical turning points, i.e. in the transition state region (marked in the figure) is enhanced. (**Right**) The probability of being in the transition state region as a function of temperature. Reproduced with permission from Öström et al. [3].

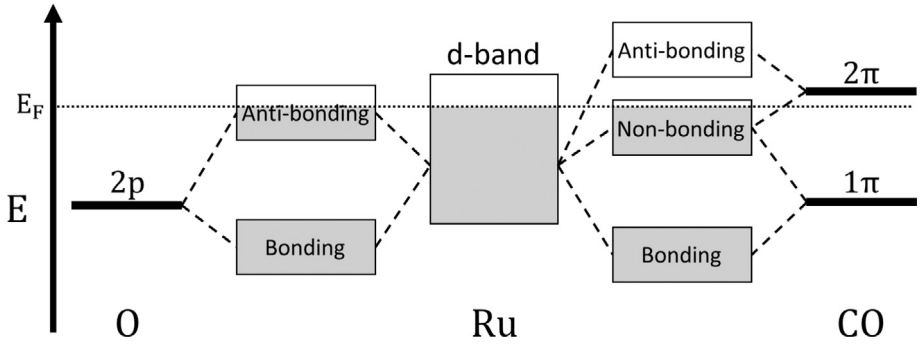

Fig. 32. Schematic of the molecular orbitals for the O—Ru and CO—Ru bonds. The antibonding Ru—O orbital and the Ru—CO nonbonding orbital cross the Fermi level. These orbitals will be further populated when conduction electrons are polarized towards the surface. The Ru—O bond will be weakened due to the partial filling of the antibonding orbital while the Ru—CO bond will be unaffected due to the nonbonding character of the orbital. Reproduced with permission from LaRue et al. [30].

of the adsorbate. The electric field vectors parallel to the surface will instead induce instantaneous surface currents.

It has been shown that intense THz pulses can be used to induce chemical reactions on a metal surface [30]. Quasi-half-cycle, broadband THz pulses with peak fields of ~1 V/nm (10 MV/cm) and a peak frequency of 10 THz were used to induce CO oxidation on the coadsorbed phase of CO and O on Ru(0001). In these studies, the electric field of the THz pulses interacted with the electron bath to steer the reaction towards CO oxidation, while shutting down the CO desorption reaction pathway. This is a significant change in the product distribution as CO desorption is the dominant reaction channel under thermal and optical laser excitation conditions [3,12–13]. In the absence of O, no desorption was found from CO/Ru(0001) due to THz irradiation, suggesting that the key to CO oxidation is the activation of the O atoms.

To study THz-induced CO oxidation, thermally programmed desorption (TPD) was used to measure surface coverages of CO and O before and after THz irradiation. Fig. 33 shows the TPD traces before and after THz irradiation of a CO/Ru(0001) surface and a CO + O/Ru(0001) surface. In the case of CO + O/Ru(0001), an additional CO TPD was performed after the surface was re-dosed with CO in order to obtain the O coverage. The adsorption sites of a saturated layer of CO, and therefore the shape of the TPD traces, are dependent on the O coverage.

The interaction of the surface O atoms with THz pulses can explain the near 100% selectivity of CO oxidation over CO desorption. The THz pulses induce oscillations in the electron density at the ruthenium surface. The oscillating electric field vector of the THz pulses will polarize the conduction band electrons in the ruthenium surface both towards and away from the surface for the duration of the THz pulse (<70 fs), depending on the sign of the electric field vector. When the electron density is shifted towards the surface, electrons will become iso-energetic with and occupy the unoccupied states of the adsorbates that are near the Fermi level, as shown in Fig. 32. In the O-metal bonding, this correlates to the filling of the antibonding orbital, weakening the O—Ru bond and increasing the bond length (Fig. 26). This occupation must last the timescale of the O-metal vibration, after which the electron can migrate back to the surface in the absence of the electric field. When the electron migrates back to the surface, the O—Ru bond will be left elongated corresponding to exciting the O atoms with large quanta of vibrational energy (see Fig. 34). These excited O atoms are mobile enough to interact with the neighboring adsorbed CO molecules, forming CO_2. For the CO-metal bonding system, the unoccupied states near the Fermi level that the electrons can occupy when the electric field pushed the electrons towards the surface is of non-bonding character. Occupation of this orbital will not destabilize the CO-metal bond and no CO will desorb from the system.

The THz pulses selectively induce CO oxidation while shutting down the dominant CO desorption reaction pathway through the polarization of the electron bath. Time-resolved XAS and XES can provide further details on the reaction dynamics and intermediate species formed on the surface. Comparing the time evolution

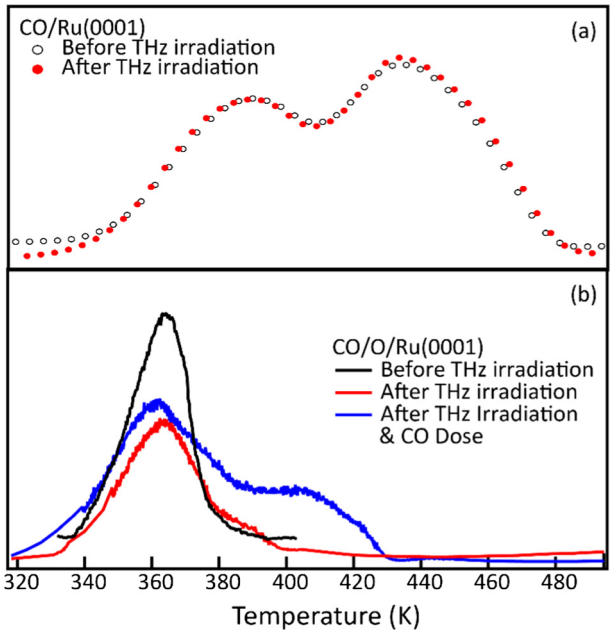

Fig. 33. CO TPD traces before and after THz irradiation for (**a**) a CO/Ru(0001) surface and (**b**) a CO + O/Ru(0001) surface. For the CO + O/Ru(0001) surface, a third TPD was performed in which CO was re-dosed onto the surface. The shape of the saturated CO TPD trace is highly dependent on the O surface coverage. This knowledge was used to obtain the O coverage in addition to the CO coverage after THz irradiation. Reproduced with permission from LaRue et al. [30].

between optical laser versus THz induced CO oxidation using time-resolved X-ray spectroscopies will lead to new insights on how to further increase the selectivity of reactions at metal interfaces. This in turn will help pave the way to designing and creating more efficient and selective catalysts.

6.5. Analysis of the chemical bonding during CO oxidation

CO oxidation on Ru(0001) has been calculated according to the reaction diagram presented in Fig. 35. In the initial state (IS), CO is chemisorbed atop in a honeycomb phase of O, *i.e.* at an oxygen coverage of 0.5 ML. As the reaction proceeds, both reactants undergo considerable displacements; at the first transition state (TS1) of the reaction, O is found at the bridge site while CO is tilting away from its original adsorption configuration. In the following, we refer to the different configurations along the reaction path by their respective number indicated in Fig. 35. In the intermediate state (IMS) in which CO_2 is weakly bound to the surface, we note a significant internal angle. Passing the second transition state

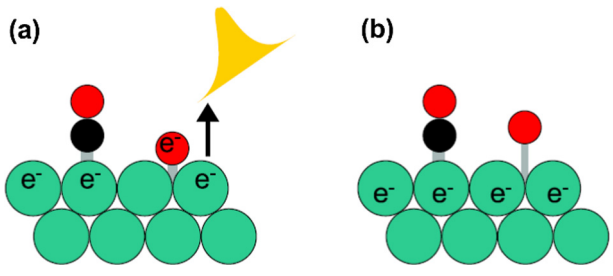

Fig. 34. In the presence of the THz field, (**a**) electrons are polarized towards the Ru surface due to the intense electric field, resulting in occupation of the Ru—O antibonding orbital, which elongates the Ru—O bond. In the absence of the THz field and (**b**) the electron transfers back to the surface, creating vibrationally excited O atoms and leading to CO oxidation. Reproduced with permission from LaRue et al. [30].

(TS2) and desorbing, CO_2 becomes linear at the final state (FS) of the reaction, in which CO_2 is in gas phase.

We start by addressing the chemical bonding of O and CO in the initial state of the reaction. To get an overview of the states involved in the reaction, we project the density of states (DOS) on the molecular orbitals of gas phase CO and the atomic orbitals of O and visualize the relevant states, *i.e.* the ones participating in the reaction.

In Fig. 36, the DOS projected on the CO 4σ, 5σ and 1π orbital (the latter is degenerate but we select the state oriented in the reaction plane) and the O p_y orbital (which is oriented along the reaction coordinate) are shown. In order to investigate the effect of co-adsorption on the electronic structure, the projected DOS of the reactants with and without co-reactant is shown. As can be seen from the peak at around −7 eV in the O projected DOS, the O p_y is slightly hybridized with the CO 5σ and 1π orbitals.

In order to follow the evolution of the different states along the reaction coordinate, the projected DOS is shown in Fig. 37, going from IS to IMS.

The most obvious observation is that, in the earlier steps, the largest changes occur for O, while only minor redistributions of density are observed in the CO projected states. We note that already in the first images, significant hybridization of the p_y orbital with the CO σ- and π-states takes place. The involvement of the 1π orbital in the reaction seems to appear slightly later, closer to the TS although there is some initial overlap observed also here. At the TS, a split of the peak corresponding to the 1π state is observed, and hybridization between CO π and σ states occurs as the bond formation with the oxygen is initialized. In order to analyze the O—CO interactions in more detail, we visualize the relevant orbitals in Figs. 38 and 39. Note that these plots are representations of the chosen states, taken at the Γ point of the Brillouin zone, and visualized in the plane along the reaction coordinate. Fig. 38 displays a state in which the CO 1π orbital and the p-orbital, denoted p_y, oriented laterally along the reaction plane, are overlapping.

We note that already in the IS configuration we have an overlap between the 1π and p_y state which we also indicated in Fig. 37. As the OC-O distance is decreased, the hybridization of the states becomes more significant and passing the TS in Image 6 a distorted (bonding) $2\sigma_u$ CO_2 orbital is beginning to form, an observation that becomes more obvious in IMS.

In Fig. 39, we instead focus on a state containing the CO 5σ and O p_y orbitals along the reaction coordinate.

Here, we see an initial hybridization of the p_y with the 5σ orbital, which becomes stronger with decreasing OC—O distance. At the TS, a new state has formed which initializes the formation of the bonding CO_2 $1\pi_u$ orbital.

Both the CO π and σ channels seem to participate in the initialization of the OC—O bond formation. To try to distinguish further the contribution in each channel, we study in Fig. 40 the charge density difference (CDD), defined as n[CO—O—Ru]—n[O—Ru]—n[CO], n being the electron density.

In the IS, the CDD resembles previous bonding mechanisms established for CO adsorbed alone on other transition metals, with a gain of charge in the π system and a loss of charge in the σ system, indicative of an overall σ to π charge transfer to minimize the Pauli repulsion in the σ channel upon adsorption [80]. Following the reaction coordinate, we notice in Image 3 charge gain in the oxygen p orbitals aligned with the surface normal (p_z). At the same time there is slight charge depletion in the CO π system, indicating CO-metal bond weakening. Moving to the TS, there is loss of charge in the O p_y orbitals, *i.e.* those parallel to the surface, while additional gain compared to Image 3 is observed in the p_z states and the onset of bond formation with CO seems to occur between the p_z orbitals and the π system of CO while the depletion in the p_y

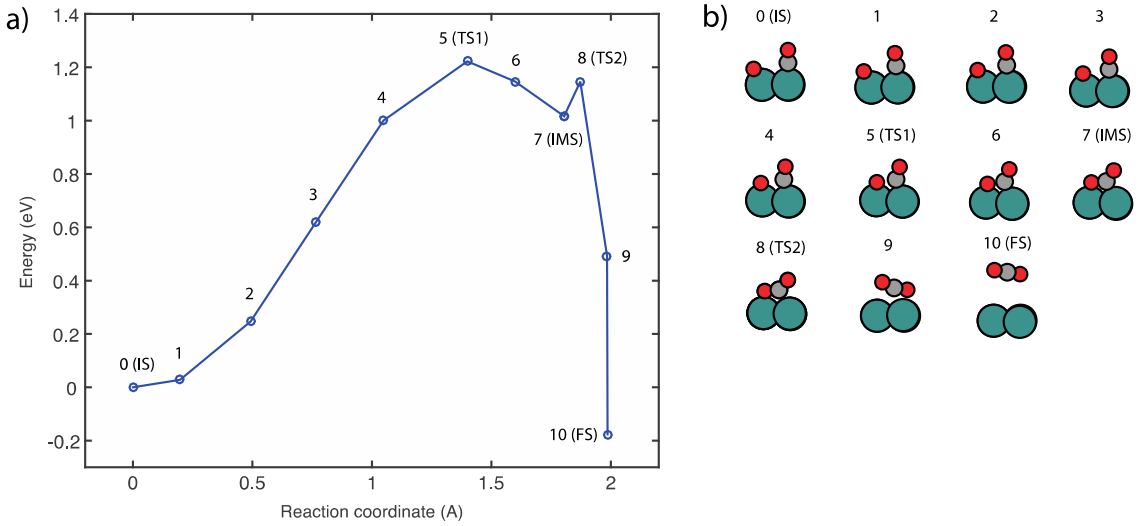

Fig. 35. (**a**) Minimum energy path (MEP) of CO oxidation on Ru(0001) starting from adsorbed O and CO, denoted the initial state (IS) which corresponds to image 0 in the sampled reaction path. The reaction passes the first transition state (TS1) to reach a metastable state of adsorbed CO_2, which we denote the intermediate state (IMS). Upon desorption of CO_2, the molecule passes a second transition state (TS2) before reaching its final state (FS) in gas phase. The structures constituting the MEP are indexed from 0 to 10 and shown in (b).

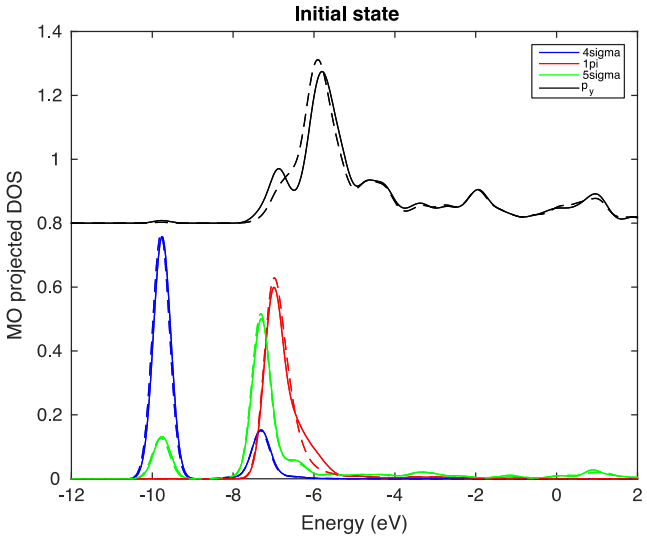

Fig. 36. Density of states (DOS) projected on selected molecular orbitals of CO (bottom part) and the p_y state of atomic O adsorbed on Ru(0001). Solid lines show the states when CO and O are co-adsorbed on the surface while dashed lines show the species in the same geometry but without the co-reactant.

orbitals is likely due to minimization of the Pauli repulsion. Towards the IMS, there is a gain of charge between OC—O, while there is still charge depletion in the p_y orbitals of the O, indicating that also in the IMS, where the bond to the metal is weak, minimizing the repulsion in the bond formation by charge transfer from σ to π is still necessary.

The last sequence of the CO oxidation reaction is desorption of weakly adsorbed CO_2 from the surface, a process associated with a small barrier of ~0.12 eV. This barrier is approximated from a constrained desorption simulation in which the CO_2—Ru is kept fixed at discrete distances while mapping out the MEP to CO_2 desorption. In Fig. 41 we show the CDD plots in this case where very little change is observed between the IMS and TS2 states. In going from TS2 to the final state the original C—O bond is rather unaffected while, when the molecule goes from the bent conformation at the surface to linear in gas phase we see a significant charge rearrangement with loss in σ and gain in π related to formation of the new bond.

7. Outlook

Here we will shortly discuss the future of probing surface chemistry and catalysis using X-ray lasers. The results in the present review, demonstrating the possibility to not only observe transient intermediates on short time scales but also species in the transition state region, point to the potential to investigate a large class of surface reactions. In particular, most of the chemistry of importance for society and industry involves C, N and O atoms and the presented spectroscopies are well suited for studying important chemical transformations involving species built on these light elements. Examples include naturally hydrogenation of CO, formation of CO from C + O, formation of NO from N + O, C—C coupling for generating fuels, NO + CO exhaust-related reactions, ammonia synthesis. The list can be made very long. On the experimental side it is important to further develop the experimental set-up in such a way as to allow to exploit polarization effects in both XAS and XES where the E-vector orientation [19] with respect to the surface can provide further information on ultrafast reorientation effects during the reaction. We also envision that scans of a longer energy range in XAS to probe shape resonances will provide further insights in terms of bond-length dependences [19,104]. Using a specific E-vector orientation we can enhance specific bond directions. Another area of development is to further use selective excitations in XES to probe only a specific subensemble of molecules [88].

Another essential development is the source itself. Even with the high intensity of the XFEL pulses, the low cross-section in these experiments gives a low count rate per pulse such that these experiments benefit greatly from high repetition-rate XFEL sources. While XFELs based on normal conducting accelerator technology, such as, *e.g.*, LCLS, SACLA, FERMI, or the upcoming SwissFEL and the Pohang XFEL are running at maximum repetition rates between ten and a few hundred pulses/s, sources which are based on superconducting accelerator technology such as FLASH (8000 pulses/s) and the European XFEL (27,000 pulses/s) can provide significantly higher repetition rates. Ultimately so-called con-

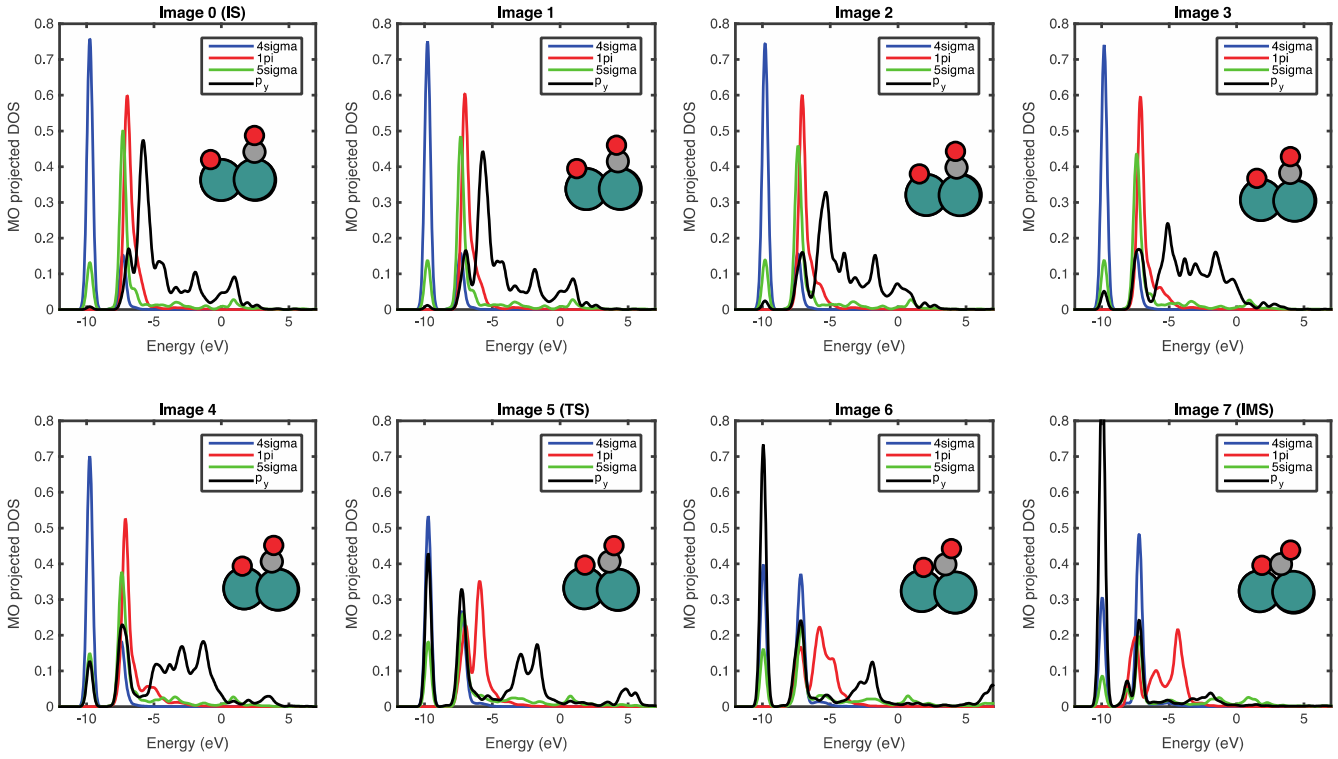

Fig. 37. Density of states (DOS) projected on selected molecular orbitals of CO (bottom part) and the p_y state of atomic O adsorbed on Ru(0001) plotted along the reaction coordinate. Image indexing is taken from Fig. 35. In order to associate the electronic structure changes with changes in the molecular orientations, the different configurations are shown as simplified structure models in each subplot.

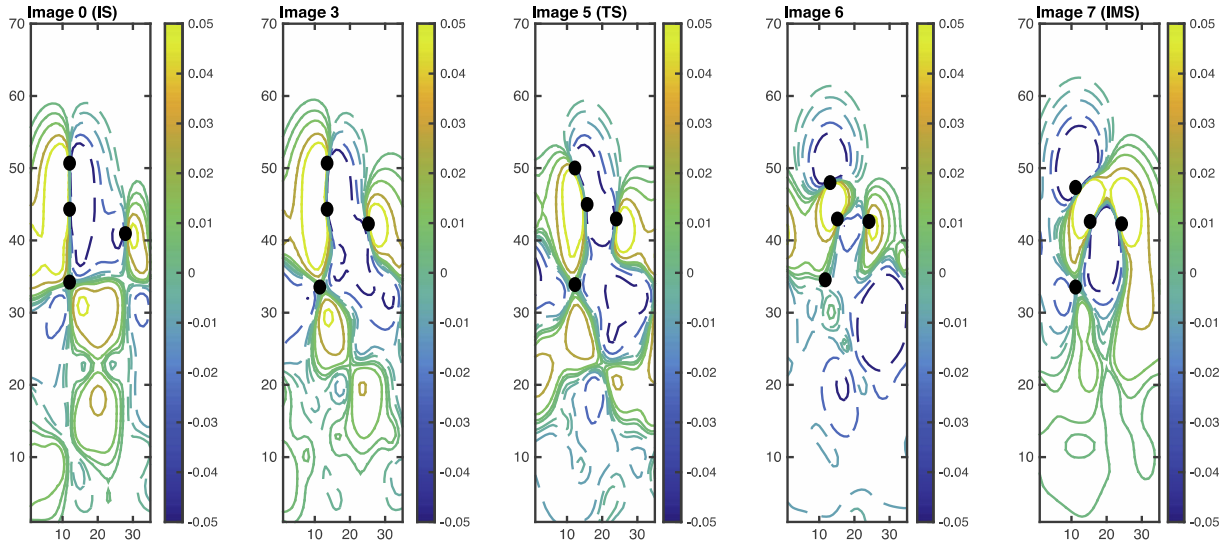

Fig. 38. A 2D cut in the reaction plane of a state consisting of overlapping CO 1π and O p_y orbitals followed along the reaction coordinate from IS over TS to IMS. The image numbers correspond to the indices in previous figures.

tinuous wave (CW) XFELs such as LCLS-II, which is under construction, or FLASH2020, the upgrade of FLASH currently under discussion, will deliver repetition rates up to 1 MHz which will be a tremendous boost for time-resolved X-ray spectroscopy techniques.

We can also envision the usage of X-ray photoelectron spectroscopy (XPS) to resolve the core electron shifts and detect various species in different adsorption sites and orientations [105,106]. The challenge is that the electrons emitted during an ultrashort X-ray pulse will repel each other and cause space charge effects such as both shifts and broadening of the spectra [107]; if the substrate is not sufficiently conductive, the build-up of positive charge during the pulse will further enhance these effects. However, reducing the intensity per pulse by orders of magnitude would limit the space charge effects making such studies feasible.

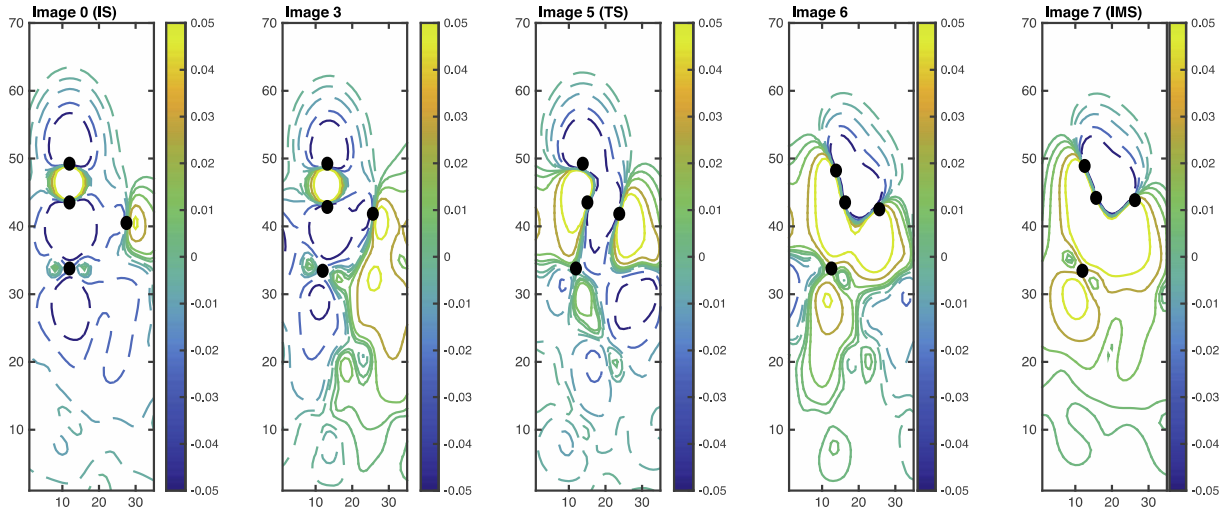

Fig. 39. A 2D cut in the reaction plane of a state consisting of overlapping CO 5σ and O p_y orbitals followed along the reaction coordinate from IS over TS to IMS. The image numbers correspond to the indices in previous figures.

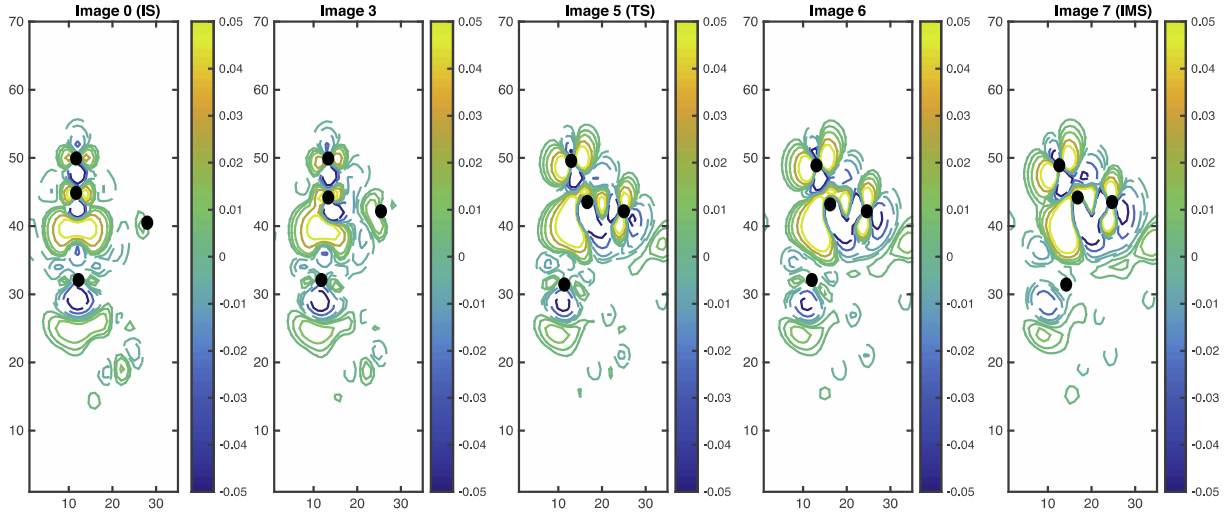

Fig. 40. Charge density difference (CDD) plots for selected structures along the reaction coordinate from IS to IMS. The CDD is calculated as n[CO—O—Ru]—n[O—Ru]—n[CO], where n is the electron density of the respective system.

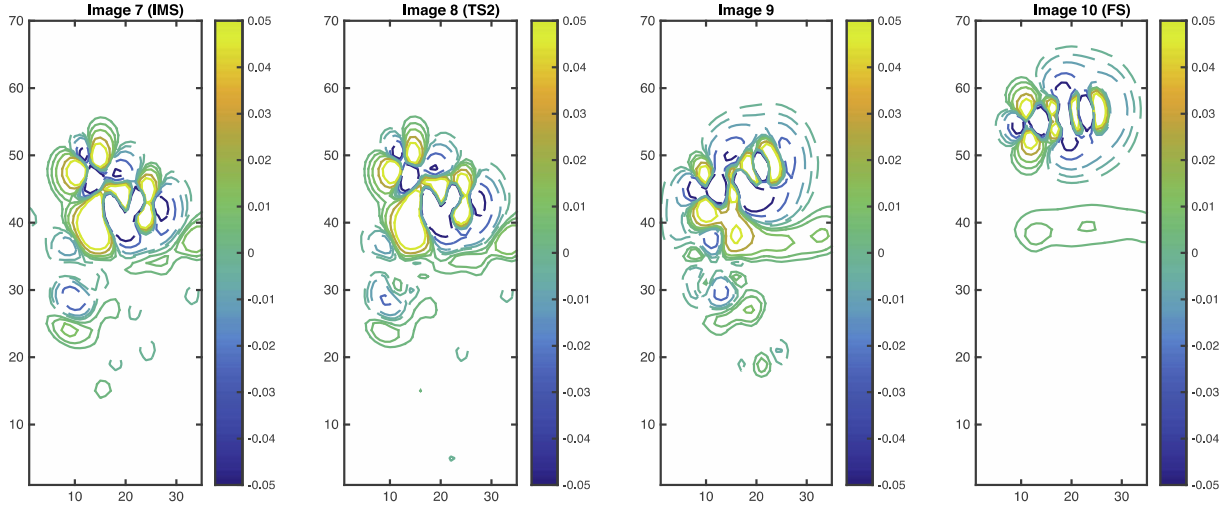

Fig. 41. Charge density difference (CDD) plots for selected structures along the reaction coordinate from IMS to FS. The CDD is calculated as n[CO—O—Ru]—n[O—Ru]—n[CO].

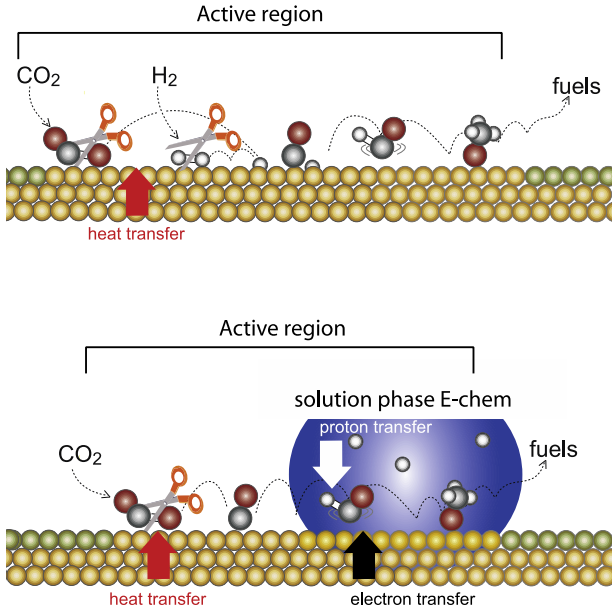

Fig. 42. Catalytic reactions involving CO_2 at the gas-solid (top) and gas-solid-liquid electrolyte (bottom) interfaces. The reactions occur on active regions on the surface of the different materials. Catalytic scission of the adsorbate by thermal energy transfer is the key elementary process of all three systems. Charge transfer across the interface is the particularity of the gas-solid-liquid electrolyte system.

Since XES and fluorescence-yield XAS are photon-in and photon-out spectroscopies and since the optical laser typically has energies below any molecular electronic transition in the gas phase, these experiments can also be carried out at high pressures. In the case of XPS, differential pumping will allow for pressures in the few torr range which can be extended to even higher pressures using photon energies in the few keV range giving rise to photoelectrons with higher kinetic energy and thus a substantially longer mean free path. Sample environments can furthermore be developed to create unique environments in terms of both single-crystal substrates and supported nanoparticles in contact either with gases or with liquids allowing for both thermally- and photo- and electro- induced chemistry, see Fig. 42. In the case of electrocatalysis the proton transfer across the interface will be an essential component to gain further insight on the dynamics of solid-liquid phase surface chemistry relevant to energy production and storage in fuel cells and artificial photosynthesis devices.

As demonstrated above it is now possible to control surface chemical reactivity using THz radiation [30]. It would be very exciting to combine THz pump and X-ray laser probe to follow the reaction on an ultrafast time scale. There is also the potential to combine the same source to generate THz radiation and X-ray laser which would provide complete internal synchronization but THz radiation may also be generated from optical sources and combined with the X-ray laser probe [108]. This would provide unique means to explore steering and guiding chemical reactions in combination with the powerful probes provided by the XFEL.

Acknowledgements

This work is supported by the Swedish Research Council, U.S. Department of Energy, Basic Energy Science through the SUNCAT Center for Interface Science and Catalysis, the Swedish Energy Agency (Energimyndigheten), the Knut and Alice Wallenberg Foundation, the U.S. Department of Energy through the SLAC Laboratory Directed Research and Development program under contract DE-AC02-76SF00515, the Volkswagen Stiftung, and the Deutsche Forschungsgemeinschaft within the excellence cluster 'Center for Ultrafast Imaging (CUI)'. The spectrum calculations were performed on resources provided by the Swedish National Infrastructure for Computing (SNIC) at the HPC2N center. Use of the Linac Coherent Light Source (LCLS), SLAC National Accelerator Laboratory, is supported by the U.S. Department of Energy, Office of Science, Office of Basic Energy Sciences under Contract No. DE-AC02-76SF00515. The SXR Instrument is funded by a consortium whose membership includes the LCLS, Stanford University through the Stanford Institute for Materials Energy Sciences (SIMES), Lawrence Berkeley National Laboratory (LBNL), University of Hamburg through the BMBF priority program FSP 301, and the Center for Free Electron Laser Science (CFEL).

References

[1] E. Worrell, D. Phylipsen, D. Einstein, N. Martin, Energy Use and Energy Intensity of the U.S., Chemical Industry, 2000.
[2] J.K. Nørskov, T. Bligaard, F. Abild-Pedersen, F. Studt, Fundamental Concepts in Heterogeneous Catalysis, Wiley, 2014.
[3] H. Öström, H. Öberg, H. Xin, J. LaRue, M. Beye, M. Dell'Angela, J. Gladh, M.L. Ng, J.A. Sellberg, S. Kaya, G. Mercurio, D. Nordlund, M. Hantschmann, F. Hieke, D. Kühn, W.F. Schlotter, G.L. Dakovski, J.J. Turner, M.P. Minitti, A. Mitra, S.P. Moeller, A. Föhlisch, M. Wolf, W. Wurth, M. Persson, J.K. Nørskov, F. Abild-Pedersen, H. Ogasawara, L.G.M. Pettersson, A. Nilsson, Probing the transition state region in catalytic CO oxidation on Ru, Science 347 (2015) 978–982.
[4] E.H.G. Backus, A. Eichler, A.W. Kleyn, M. Bonn, Real-time observation of molecular motion on a surface, Science 310 (5755) (2005) 1790–1793.
[5] L. Bartels, F. Wang, D. Möller, E. Knoesel, T.F. Heinz, Real-space observation of molecular motion induced by femtosecond laser pulses, Science 305 (2004) 648.
[6] M. Bauer, C. Lei, K. Read, R. Tobey, J. Gland, M.M. Murnane, H.C. Kapteyn, Direct observation of surface chemistry using ultrafast soft-X-ray pulses, Phys. Rev. Lett. 87 (2) (2001) 025501.
[7] I.M. Fane, D.A. King, Z.P. Liu, H. Arnolds, Real Time observation of nonadiabatic surface dynamics: the first picosecond in the dissociaton of NO on iridium, Phys. Rev. Lett. 97 (2006) 186105.
[8] C. Frischkorn, M. Wolf, Femtochemistry at metal surfaces: nonadiabatic reaction dynamics, Chem. Rev. 106 (10) (2006) 4207–4233.
[9] A.C. Luntz, The dynamics of making and breaking bonds at surfaces, in: A. Nilsson, L.G.M. Pettersson, J.K. Norskov (Eds.), Chemical Bonding at Surfaces and Interfaces, Elsevier, 2008.
[10] J.C. Tully, Chemical dynamics at metal surfaces, Ann. Revs, Phys. Chem. 51 (2000) 153.
[11] M. Lisowski, P.A. Loukakos, U. Bovensiepen, J. Stähler, C. Gahl, M. Wolf, Ultrafast dynamics of electron thermalization, cooling and transport effects in Ru (001), Appl. Phys. A 78 (2004) 165–176.
[12] H. Öberg, J. Gladh, K. Marks, H. Ogasawara, A. Nilsson, L.G.M. Pettersson, H. Öström, Indication of non-thermal contribution to visible femtosecond laser-induced CO oxidation on Ru(0001), J. Chem. Phys. 143 (7) (2015) 074701.
[13] M. Bonn, S. Funk, C. Hess, D.N. Denzler, C. Stampfl, M. Scheffler, M. Wolf, G. Ertl, Phonon- versus electron-mediated desorption and oxidation of CO on Ru (0001), Science 285 (5430) (1999) 1042–1045.
[14] I.M. Lane, D.A. King, Z.-P. Liu, H. Arnolds, Real-time observation of nonadiabatic surface dynamics: the first picosecond in the dissociation of NO on iridium, Phys. Rev. Lett. 97 (2006) 186105.
[15] M. Bonn, C. Hess, S. Funk, J.H. Miners, B.N.J. Persson, M. Wolf, G. Ertl, Femtosecond surface vibrational spectroscopy of CO adsorbed on Ru(001) during desorption, Phys. Rev. Lett. 84 (20) (2000) 4653–4656.
[16] F. Fournier, W. Zheng, S. Carrez, H. Dubost, B. Bourguignon, Vibrational dynamics of adsorbed molecules under conditions of photodesorption: pump-probe SFG spectra of CO/Pt(111), J. Chem. Phys. 121 (10) (2004) 4839–4847.
[17] K. Inoue, K. Watanabe, Y. Matsumoto, Instantaneous vibrational frequencies of diffusing and desorbing adsorbates: CO/Pt(111), J. Chem. Phys. 137 (2) (2012).
[18] H. Dachraoui, M. Michelswirth, P. Siffalovic, P. Bartz, C. Schäfer, B. Schnatwinkel, J. Mattay, W. Pfeiffer, M. Drescher, U. Heinzmann, Photoinduced reconfiguration cycle in a molecular adsorbate layer studied by femtosecond inner-shell photoelectron spectroscopy, Phys. Rev. Lett. 106 (2011) 107401.
[19] J. Stöhr, NEXAFS Spectroscopy, Springer-Verlag, Heidelberg, 1991.
[20] A. Nilsson, L.G.M. Pettersson, Adsorbate electronic structure and bonding on metal surfaces, in: A. Nilsson, L.G.M. Pettersson, J.K. Nørskov (Eds.), Chemical Bonding at Surfaces and Interfaces, Elsevier, Amsterdam, 2008, pp. 57–142.
[21] A. Nilsson, L.G.M. Pettersson, Chemical bonding on surfaces probed by X-ray emission spectroscopy and density functional theory, Surf. Sci. Rep. 55 (2–5) (2004) 49–167.
[22] A. Nilsson, J. Hasselström, A. Föhlisch, O. Karis, L.G.M. Pettersson, M. Nyberg, L. Triguero, Probing chemical bonding in adsorbates using X-ray emission spectroscopy, J. Electr. Spectrosc. Rel. Phen. 110 (1–3) (2000) 15–39.

[23] J. Hasselström, O. Karis, M. Nyberg, L.G.M. Pettersson, M. Weinelt, N. Wassdahl, A. Nilsson, The bonding and electronic structure changes upon adsorption of important functional groups: glycine on copper, J. Phys. Chem. B 104 (48) (2000) 11480–11483.

[24] W. Ackermann, G. Asova, V. Ayvazyan, A. Azima, N. Baboi, J. Bahr, V. Balandin, B. Beutner, A. Brandt, A. Bolzmann, R. Brinkmann, O.I. Brovko, M. Castellano, P. Castro, L. Catani, E. Chiadroni, S. Choroba, A. Cianchi, J.T. Costello, D. Cubaynes, J. Dardis, W. Decking, H. Delsim-Hashemi, A. Delserieys, G. Di Pirro, M. Dohlus, S. Dusterer, A. Eckhardt, H.T. Edwards, B. Faatz, J. Feldhaus, K. Flottmann, J. Frisch, L. Frohlich, T. Garvey, U. Gensch, C. Gerth, M. Gorler, N. Golubeva, H.J. Grabosch, M. Grecki, O. Grimm, K. Hacker, U. Hahn, J.H. Han, K. Honkavaara, T. Hott, M. Huning, Y. Ivanisenko, E. Jaeschke, W. Jalmuzna, T. Jezynski, R. Kammering, V. Katalev, K. Kavanagh, E.T. Kennedy, S. Khodyachykh, K. Klose, V. Kocharyan, M. Korfer, M. Kollewe, W. Koprek, S. Korepanov, D. Kostin, M. Krassilnikov, G. Kube, M. Kuhlmann, C.L.S. Lewis, L. Lilje, T. Limberg, D. Lipka, F. Lohl, H. Luna, M. Luong, M. Martins, M. Meyer, P. Michelato, V. Miltchev, W.D. Moller, L. Monaco, W.F.O. Muller, A. Napieralski, O. Napoly, P. Nicolosi, D. Nolle, T. Nunez, A. Oppelt, C. Pagani, R. Paparella, N. Pchalek, J. Pedregosa-Gutierrez, B. Petersen, B. Petrosyan, G. Petrosyan, L. Petrosyan, J. Pfluger, E. Plonjes, L. Poletto, K. Pozniak, E. Prat, D. Proch, P. Pucyk, P. Radcliffe, H. Redlin, K. Rehlich, M. Richter, M. Roehrs, J. Roensch, R. Romaniuk, M. Ross, J. Rossbach, V. Rybnikov, M. Sachwitz, E.L. Saldin, W. Sandner, H. Schlarb, B. Schmidt, M. Schmitz, P. Schmuser, J.R. Schneider, E.A. Schneidmiller, S. Schnepp, S. Schreiber, M. Seidel, D. Sertore, A.V. Shabunov, C. Simon, S. Simrock, E. Sombrowski, A.A. Sorokin, P. Spanknebel, R. Spesyvtsev, L. Staykov, B. Steffen, F. Stephan, F. Stulle, H. Thom, K. Tiedtke, M. Tischer, S. Toleikis, R. Treusch, D. Trines, I. Tsakov, E. Vogel, T. Weiland, H. Weise, M. Wellhoffer, M. Wendt, I. Will, A. Winter, K. Wittenburg, W. Wurth, P. Yeates, M.V. Yurkov, I. Zagorodnov, K. Zapfe, Operation of a free-electron laser from the extreme ultraviolet to the water window, Nat. Photon. 1 (6) (2007) 336–342.

[25] P. Emma, R. Akre, J. Arthur, R. Bionta, C. Bostedt, J. Bozek, A. Brachmann, P. Bucksbaum, R. Coffee, F.J. Decker, Y. Ding, D. Dowell, S. Edstrom, A. Fisher, J. Frisch, S. Gilevich, J. Hastings, G. Hays, P. Hering, Z. Huang, R. Iverson, H. Loos, M. Messerschmidt, A. Miahnahri, S. Moeller, H.D. Nuhn, G. Pile, D. Ratner, J. Rzepiela, D. Schultz, T. Smith, P. Stefan, H. Tompkins, J. Turner, J. Welch, W. White, J. Wu, G. Yocky, J. Galayda, First lasing and operation of an angstrom-wavelength free-electron laser, Nat. Photon. 4 (9) (2010) 641–647.

[26] T. Ishikawa, H. Aoyagi, T. Asaka, Y. Asano, N. Azumi, T. Bizen, H. Ego, K. Fukami, T. Fukui, Y. Furukawa, S. Goto, H. Hanaki, T. Hara, T. Hasegawa, T. Hatsui, A. Higashiya, T. Hirono, N. Hosoda, M. Ishii, T. Inagaki, Y. Inubushi, T. Itoga, Y. Joti, M. Kago, T. Kameshima, H. Kimura, Y. Kirihara, A. Kiyomichi, T. Kobayashi, C. Kondo, T. Kudo, H. Maesaka, X.M. Marechal, T. Masuda, S. Matsubara, T. Matsumoto, T. Matsushita, S. Matsui, M. Nagasono, N. Nariyama, H. Ohashi, T. Ohata, T. Ohshima, S. Ono, Y. Otake, C. Saji, T. Sakurai, T. Sato, K. Sawada, T. Seike, K. Shirasawa, T. Sugimoto, S. Suzuki, S. Takahashi, H. Takebe, K. Takeshita, K. Tamasaku, H. Tanaka, R. Tanaka, T. Tanaka, T. Togashi, K. Togawa, A. Tokuhisa, H. Tomizawa, K. Tono, S.K. Wu, M. Yabashi, M. Yamaga, A. Yamashita, K. Yanagida, C. Zhang, T. Shintake, H. Kitamura, N. Kumagai, A compact X-ray free-electron laser emitting in the sub-angstrom region, Nat. Photon. 6 (8) (2012) 540–544.

[27] E. Allaria, R. Appio, L. Badano, W.A. Barletta, S. Bassanese, S.G. Biedron, A. Borga, E. Busetto, D. Castronovo, P. Cinquegrana, S. Cleva, D. Cocco, M. Cornacchia, P. Craievich, I. Cudin, G. D'Auria, M. Dal Forno, M.B. Danailov, R. De Monte, G. De Ninno, P. Delgiusto, A. Demidovich, S. Di Mitri, B. Diviacco, A. Fabris, R. Fabris, W. Fawley, M. Ferianis, E. Ferrari, S. Ferry, L. Froehlich, P. Furlan, G. Gaio, F. Gelmetti, L. Giannessi, M. Giannini, R. Gobessi, R. Ivanov, E. Karantzoulis, M. Lonza, A. Lutman, B. Mahieu, M. Milloch, S.V. Milton, M. Musardo, I. Nikolov, S. Noe, F. Parmigiani, G. Penco, M. Petronio, L. Pivetta, M. Predonzani, F. Rossi, L. Rumiz, A. Salom, C. Scafuri, C. Serpico, P. Sigalotti, S. Spampinati, C. Spezzani, M. Svandrlik, C. Svetina, S. Tazzari, M. Trovo, R. Umer, A. Vascotto, M. Veronese, R. Visintini, M. Zaccaria, D. Zangrando, M. Zangrando, Highly coherent and stable pulses from the FERMI seeded free-electron laser in the extreme ultraviolet, Nat. Photon. 6 (10) (2012) 699–704.

[28] C. Bostedt, S. Boutet, D.M. Fritz, Z.R. Huang, H.J. Lee, H.T. Lemke, A. Robert, W. F. Schlotter, J.J. Turner, G.J. Williams, Linac Coherent Light Source: The first five years, Rev. Mod. Phys. 88 (1) (2016) 015007.

[29] C. Bostedt, H.N. Chapman, J.T. Costello, J.R.C. Lopez-Urrutia, S. Dusterer, S.W. Epp, J. Feldhaus, A. Föhlisch, M. Meyer, T. Moller, R. Moshammer, M. Richter, K. Sokolowski-Tinten, A. Sorokin, K. Tiedtke, J. Ullrich, W. Wurth, Experiments at FLASH, Nucl. Instrum. Meth. Phys. Res. Sect. A-Accel. Spectrom. Detect. Assoc. Equip. 601 (1–2) (2009) 108–122.

[30] J.L. LaRue, T. Katayama, A. Lindenberg, A.S. Fisher, H. Öström, A. Nilsson, H. Ogasawara, THz-pulse-induced selective catalytic CO oxidation on Ru, Phys. Rev. Lett. 115 (3) (2015) 036103.

[31] M. Dell'Angela, T. Anniyev, M. Beye, R. Coffee, A. Föhlisch, J. Gladh, T. Katayama, S. Kaya, O. Krupin, J. LaRue, A. Møgelhøj, D. Nordlund, J.K. Nørskov, H. Öberg, H. Ogasawara, H. Öström, L.G.M. Pettersson, W.F. Schlotter, J.A. Sellberg, F. Sorgenfrei, J.J. Turner, M. Wolf, W. Wurth, A. Nilsson, Real-time observation of surface bond breaking with an X-ray laser, Science 339 (6125) (2013) 1302–1305.

[32] H. Xin, J. LaRue, H. Öberg, M. Beye, M. Dell'Angela, J.J. Turner, J. Gladh, M.L. Ng, J.A. Sellberg, S. Kaya, G. Mercurio, F. Hieke, D. Nordlund, W.F. Schlotter, G.L. Dakovski, M.P. Minitti, A. Föhlisch, M. Wolf, W. Wurth, H. Ogasawara, J.K. Nørskov, H. Öström, L.G.M. Pettersson, A. Nilsson, F. Abild-Pedersen, Strong influence of coadsorbate interaction on CO desorption dynamics on Ru(0001) probed by ultrafast X-Ray spectroscopy and *ab initio* simulations, Phys. Rev. Lett. 114 (15) (2015) 156101.

[33] M. Beye, H. Öberg, H. Xin, G.L. Dakovski, M. Dell'Angela, A. Föhlisch, J. Gladh, M. Hantschmann, F. Hieke, S. Kaya, D. Kühn, J. LaRue, G. Mercurio, M.P. Minitti, A. Mitra, S.P. Moeller, M.L. Ng, A. Nilsson, D. Nordlund, J. Nørskov, H. Öström, H. Ogasawara, M. Persson, W.F. Schlotter, J.A. Sellberg, M. Wolf, F. Abild-Pedersen, L.G.M. Pettersson, W. Wurth, Chemical bond activation observed with an X-ray laser, J. Phys. Chem. Lett. 7 (18) (2016) 3647–3651.

[34] I. Chorkendorff, Private communication 2000.

[35] Z. Huang, in: Proceedings of the 4th International Particle Accelerator Conference, Shanghaikrjg, 2013.

[36] H. Öberg, J. Gladh, M. Dell'Angela, T. Anniyev, M. Beye, R. Coffee, A. Föhlisch, T. Katayama, S. Kaya, J. LaRue, A. Møgelhøj, D. Nordlund, H. Ogasawara, W.F. Schlotter, J.A. Sellberg, F. Sorgenfrei, J.J. Turner, M. Wolf, W. Wurth, H. Öström, A. Nilsson, J.K. Nørskov, L.G.M. Pettersson, Optical laser-induced CO desorption from Ru(0001) monitored with a free-electron X-ray laser: DFT prediction and X-ray confirmation of a precursor state, Surf. Sci. 640 (2015) 80–88.

[37] R. Clauberg, A. Blacha, High electron-density effects in electron spectroscopies - consequences for picosecond photoemission and electron-beam sampling, J. Appl. Phys. 65 (11) (1989) 4095–4106.

[38] T.L. Gilton, J.P. Cowin, G.D. Kubiak, A.V. Hamza, Intense surface photoemission - space-charge effects and self-acceleration, J. Appl. Phys. 68 (9) (1990) 4802–4810.

[39] X.J. Zhou, B. Wannberg, W.L. Yang, V. Brouet, Z. Sun, J.F. Douglas, D. Dessau, Z. Hussain, Z.X. Shen, Space charge effect and mirror charge effect in photoemission spectroscopy, J. Electron Spectrosc. Rel. Phenom. 142 (1) (2005) 27–38.

[40] S. Passlack, S. Mathias, O. Andreyev, D. Mittnacht, M. Aeschlimann, M. Bauer, Space charge effects in photoemission with a low repetition, high intensity femtosecond laser source, J. Appl. Phys. 100 (2) (2006) 024912.

[41] S. Hellmann, K. Rossnagel, M. Marczynski-Buehlow, L. Kipp, Vacuum space-charge effects in solid-state photoemission, Phys. Rev. B 79 (3) (2009) 035402.

[42] F. Gel'mukhanov, H. Ågren, Resonant X-ray Raman scattering, Phys. Rep.-Rev. Sect. Phys. Lett. 312 (3–6) (1999) 87–330.

[43] L. Triguero, A. Föhlisch, P. Väterlein, J. Hasselström, M. Weinelt, L.G.M. Pettersson, Y. Luo, H. Ågren, A. Nilsson, Direct experimental measurement of donation/back-donation in unsaturated hydrocarbon bonding to metals, J. Am. Chem. Soc. 122 (49) (2000) 12310–12316.

[44] H. Ogasawara, B. Brena, D. Nordlund, M. Nyberg, A. Pelmenschikov, L.G.M. Pettersson, A. Nilsson, Structure and bonding of water on Pt(111), Phys. Rev. Lett. 89 (2002) 276102.

[45] M. Beye, O. Krupin, G. Hays, A.H. Reid, D. Rupp, S. de Jong, S. Lee, W.S. Lee, Y.D. Chuang, R. Coffee, J.P. Cryan, J.M. Glownia, A. Föhlisch, M.R. Holmes, A.R. Fry, W.E. White, C. Bostedt, A.O. Scherz, H.A. Durr, W.F. Schlotter, X-ray pulse preserving single-shot optical cross-correlation method for improved experimental temporal resolution, Appl. Phys. Lett. 100 (12) (2012) 121108.

[46] T. Katayama, T. Anniyev, M. Beye, R. Coffee, M. Dell'Angela, A. Föhlisch, J. Gladh, S. Kaya, O. Krupin, A. Nilsson, D. Nordlund, W.F. Schlotter, J.A. Sellberg, F. Sorgenfrei, J.J. Turner, W. Wurth, H. Öström, H. Ogasawara, Ultrafast soft X-ray emission spectroscopy of surface adsorbates using an X-ray free electron laser, J. Electron Spectrosc. Rel. Phenom. 187 (2013) 9–14.

[47] W.F. Schlotter, J.J. Turner, M. Rowen, P. Heimann, M. Holmes, O. Krupin, M. Messerschmidt, S. Moeller, J. Krzywinski, R. Soufli, M. Fernández-Perea, N. Kelez, S. Lee, R. Coffee, G. Hays, M. Beye, N. Gerken, F. Sorgenfrei, S. Hau-Riege, L. Juha, J. Chalupsky, V. Hajkova, A.P. Mancuso, A. Singer, O. Yefanov, I.A. Vartanyants, G. Cadenazzi, B. Abbey, K.A. Nugent, H. Sinn, J. Lüning, S. Schaffert, S. Eisebitt, W.-S. Lee, A. Scherz, A.R. Nilsson, W. Wurth, The soft X-ray instrument for materials studies at the linac coherent light source X-ray free-electron laser, Rev. Scient. Instrum. 83 (4) (2012) 043107.

[48] V. Hajkova, L. Juha, P. Bohacek, T. Burian, J. Chalupsky, L. Vysin, J. Gaudin, P.A. Heimann, S.P. Hau-Riege, M. Jurek, D. Klinger, J. Pelka, R. Sobierajski, J. Krzywinski, M. Messerschmidt, S.P. Moeller, B. Nagler, M. Rowen, W.F. Schlotter, M.L. Swiggers, J.J. Turner, S.M. Vinko, T. Whitcher, J. Wark, M. Matuchova, S. Bajt, H. Chapman, T. Dzelzainis, D. Riley, J. Andreasson, J. Hajdu, B. Iwan, N. Timneanu, K. Saksl, R. Faeustlin, A. Singer, K. Tiedtke, S. Toleikis, I. Vartaniants, H. Wabnitz, X-ray laser-induced ablation of lead compounds, in: L. Juha, S. Bajt, R.A. London (Eds.), Damage to Vuv, Euv, and X-Ray Optics III, vol. 8077, 2011.

[49] P. Schmüser, M. Dohlus, J. Rossbach, C. Behrens, Free-Electron Laser in the Ultraviolet and X-Ray Regime, vol. 258, Springer International Publishing, Switzerland, 2014.

[50] P. Heimann, O. Krupin, W.F. Schlotter, J. Turner, J. Krzywinski, F. Sorgenfrei, M. Messerschmidt, D. Bernstein, J. Chalupsky, V. Hajkova, S. Hau-Riege, M. Holmes, L. Juha, N. Kelez, J. Luening, D. Nordlund, M. Fernandez Perea, A. Scherz, R. Soufli, W. Wurth, M. Rowen, Linac coherent light source soft X-ray materials science instrument optical design and monochromator commissioning, Rev. Scient. Instrum. 82 (9) (2011) 093104.

[51] M. Wellhöfer, M. Martins, W. Wurth, A.A. Sorokin, M. Richter, Performance of the monochromator beamline at FLASH, J. Optics A-Pure Appl. Optics 9 (7) (2007) 749–756.

[52] C. Gahl, A. Azima, M. Beye, M. Deppe, K. Doebrich, U. Hasslinger, F. Hennies, A. Melnikov, M. Nagasono, A. Pietzsch, M. Wolf, W. Wurth, A. Foehlisch, A femtosecond X-ray/optical cross-correlator, Nat. Photon. 2 (3) (2008) 165–169.

[53] T. Maltezopoulos, S. Cunovic, M. Wieland, M. Beye, A. Azima, H. Redlin, M. Krikunova, R. Kalms, U. Fruhling, F. Budzyn, W. Wurth, A. Föhlisch, M. Drescher, Single-shot timing measurement of extreme-ultraviolet free-electron laser pulses, New J. Phys. 10 (2008) 033026.

[54] O. Krupin, M. Trigo, W.F. Schlotter, M. Beye, F. Sorgenfrei, J.J. Turner, D.A. Reis, N. Gerken, S. Lee, W.S. Lee, G. Hays, Y. Acremann, B. Abbey, R. Coffee, M. Messerschmidt, S.P. Hau-Riege, G. Lapertot, J. Luning, P. Heimann, R. Soufli, M. Fernandez-Perea, M. Rowen, M. Holmes, S.L. Molodtsov, A. Föhlisch, W. Wurth, Temporal cross-correlation of X-ray free electron and optical lasers using soft X-ray pulse induced transient reflectivity, Opt. Exp. 20 (10) (2012) 11396–11406.

[55] B. Hammer, J.K. Nørskov, Why gold is the noblest of all the metals, Nature 376 (6537) (1995) 238–240.

[56] F. Abild-Pedersen, J. Greeley, F. Studt, J. Rossmeisl, T.R. Munter, P.G. Moses, E. Skulason, T. Bligaard, J.K. Nørskov, Scaling properties of adsorption energies for hydrogen-containing molecules on transition-metal surfaces, Phys. Rev. Lett. 99 (1) (2007).

[57] J.K. Nørskov, T. Bligaard, A. Logadottir, S. Bahn, L.B. Hansen, M. Bollinger, H. Bengaard, B. Hammer, Z. Sljivancanin, M. Mavrikakis, Y. Xu, S. Dahl, C.J.H. Jacobsen, Universality in heterogeneous catalysis, J. Catal. 209 (2) (2002) 275–278.

[58] J. Enkovaara, C. Rostgaard, J.J. Mortensen, J. Chen, M. Dułak, L. Ferrighi, J. Gavnholt, C. Glinsvad, V. Haikola, H.A. Hansen, H.H. Kristoffersen, M. Kuisma, A.H. Larsen, L. Lehtovaara, M. Ljungberg, O. Lopez-Acevedo, P.G. Moses, J. Ojanen, T. Olsen, V. Petzold, N.A. Romero, J. Stausholm-Møller, M. Strange, G. A. Tritsaris, M. Vanin, M. Walter, B. Hammer, H. Häkkinen, G.K.H. Madsen, R. M. Nieminen, J.K. Nørskov, M. Puska, T.T. Rantala, J. Schiøtz, K.S. Thygesen, K. W. Jacobsen, Electronic structure calculations with GPAW: a real-space implementation of the projector augmented-wave method, J. Phys.: Cond. Matter 22 (25) (2010) 253202.

[59] J.J. Mortensen, L.B. Hansen, K.W. Jacobsen, Real-space grid implementation of the projector augmented wave method, Phys. Rev. B 71 (3) (2005) 035109.

[60] P. Giannozzi, S. Baroni, N. Bonini, M. Calandra, R. Car, C. Cavazzoni, D. Ceresoli, G.L. Chiarotti, M. Cococcioni, I. Dabo, A.D. Corso, S.d. Gironcoli, S. Fabris, G. Fratesi, R. Gebauer, U. Gerstmann, C. Gougoussis, A. Kokalj, M. Lazzeri, L. Martin-Samos, N. Marzari, F. Mauri, R. Mazzarello, S. Paolini, A. Pasquarello, L. Paulatto, C. Sbraccia, S. Scandolo, G. Sclauzero, A.P. Seitsonen, A. Smogunov, P. Umari, R.M. Wentzcovitch, Quantum Espresso: a modular and open-source software project for quantum simulations of materials, J. Phys.: Cond. Matter 21 (39) (2009) 395502.

[61] J. Wellendorff, K.T. Lundgaard, A. Møgelhøj, V. Petzold, D.D. Landis, J.K. Nørskov, T. Bligaard, K.W. Jacobsen, Density functionals for surface science: Exchange-correlation model development with Bayesian error estimation, Phys. Rev. B 85 (23) (2012) 235149.

[62] G. Henkelman, B.P. Uberuaga, H. Jonsson, A climbing image nudged elastic band method for finding saddle points and minimum energy paths, J. Chem. Phys. 113 (22) (2000) 9901–9904.

[63] https://wiki.fysik.dtu.dk/ase/ase/thermochemistry/thermochemistry.html.

[64] D.J. Doren, J.C. Tully, Precursor-mediated adsorption and desorption - a theoretical-analysis, Langmuir 4 (2) (1988) 256–268.

[65] D.J. Doren, J.C. Tully, Dynamics of precursor-mediated chemisorption, J. Chem. Phys. 94 (12) (1991) 8428–8440.

[66] P.S. Bagus, K. Hermann, C.W. Bauschlicher, A new analysis of charge-transfer and polarization for ligand-metal bonding - model studies of Al_4CO and Al_4NH_3, J. Chem. Phys. 80 (9) (1984) 4378–4386.

[67] G. Blyholder, Molecular orbital view of chemisorbed carbon monoxide, J. Phys. Chem. 68 (10) (1964) 2772.

[68] A. Föhlisch, M. Nyberg, J. Hasselström, O. Karis, L.G.M. Pettersson, A. Nilsson, How carbon monoxide adsorbs in different sites, Phys. Rev. Lett. 85 (15) (2000) 3309–3312.

[69] A. Föhlisch, M. Nyberg, P. Bennich, L. Triguero, J. Hasselström, O. Karis, L.G.M. Pettersson, A. Nilsson, The bonding of CO to metal surfaces, J. Chem. Phys. 112 (4) (2000) 1946–1958.

[70] L. Pettersson, A. Nilsson, A molecular perspective on the d-band model: synergy between experiment and theory, Top. Catal. 57 (1–4) (2014) 2–13.

[71] M.P. Ljungberg, J.J. Mortensen, L.G.M. Pettersson, An implementation of core level spectroscopies in a real space projector augmented wave density functional theory code, J. Electron Spectrosc. Rel. Phenom. 184 (8–10) (2011) 427–439.

[72] A. Föhlisch, J. Hasselström, P. Bennich, N. Wassdahl, O. Karis, A. Nilsson, L. Triguero, M. Nyberg, L.G.M. Pettersson, Ground-state interpretation of X-ray emission spectroscopy on adsorbates: CO adsorbed on Cu(100), Phys. Rev. B 61 (23) (2000) 16229–16240.

[73] K. Hermann, L.G.M. Pettersson, M.E.D.C. Casida, A. Goursot, A. Koester, A. St-Amant, D.R. Salahub, V. Carravetta, A. Duarte, N. Godbout, J. Guan, C. Jamorski, M. Leboeuf, M. Leetmaa, M. Nyberg, L. Pedocchi, F. Sim, L. Triguero, A. Vela, StoBe-deMon Software, 2014.

[74] L. Triguero, L.G.M. Pettersson, H. Ågren, Calculations of near-edge X-ray-absorption spectra of gas-phase and chemisorbed molecules by means of density-functional and transition-potential theory, Phys. Rev. B 58 (12) (1998) 8097–8110.

[75] M. Leetmaa, M.P. Ljungberg, A. Lyubartsev, A. Nilsson, L.G.M. Pettersson, Theoretical approximations to X-ray absorption spectroscopy of liquid water and ice, J. Electron Spectrosc. Rel. Phenom. 177 (2–3) (2010) 135–157.

[76] A.D. Becke, Density-functional exchange-energy approximation with corrects asymptotic-behavior, Phys. Rev. A 38 (6) (1988) 3098–3100.

[77] J.P. Perdew, Density-functional approximation for the correlation-energy of the inhomogeneous electron-gas, Phys. Rev. B 33 (12) (1986) 8822–8824.

[78] O. Takahashi, L.G.M. Pettersson, Functional dependence of core-excitation energies, J. Chem. Phys. 121 (21) (2004) 10339–10345.

[79] A. Föhlisch, W. Wurth, M. Stichler, C. Keller, A. Nilsson, X-ray emission spectroscopy of (2 root 3 × 2 root 3)R30 degrees CO/Ru(0001): Comparison to c(2 × 2) CO/Ni(100) and c(2 × 2)CO/Cu(100), J. Chem. Phys. 121 (10) (2004) 4848–4852.

[80] M. Nyberg, A. Föhlisch, L. Triguero, A. Bassan, A. Nilsson, L.G.M. Pettersson, Bonding in metal-carbonyls: a comparison with experiment and calculations on adsorbed CO, J. Molec. Struct.-Theochem 762 (1–3) (2006) 123–132.

[81] K.P. Huber, G. Herzberg, Constants of Diatomic Molecules, vol. IV, Van Nostrand Reinhold, New York, 1979.

[82] S. Funk, M. Bonn, D.N. Denzler, C. Hess, M. Wolf, G. Ertl, Desorption of CO from Ru(001) induced by near-infrared femtosecond laser pulses, J. Chem. Phys. 112 (22) (2000) 9888–9897.

[83] J. Gladh, T. Hansson, H. Öström, Electron- and phonon-coupling in femtosecond laser-induced desorption of CO from Ru(0001), Surf. Sci. 615 (2013) 65–71.

[84] P. Skytt, P. Glans, K. Gunnelin, J.H. Guo, J. Nordgren, Y. Luo, H. Ågren, Role of screening and angular distributions in resonant X-ray emission of CO, Phys. Rev. A 55 (1) (1997) 134–145.

[85] A. Cassuto, D.A. King, Rate expressions for adsorption and desorption-kinetics with precursor states and lateral interactions, Surf. Sci. 102 (2–3) (1981) 388–404.

[86] P. Kisliuk, The sticking probabilities of gases chemisorbed on the surfaces of solids, J. Phys. Chem. Solids 3 (1–2) (1957) 95–101.

[87] J.B. Taylor, I. Langmuir, The evaporation of atoms, ions and electrons from caesium films on tungsten, Phys. Rev. 44 (6) (1933) 423–458.

[88] M. Beye, T. Anniyev, R. Coffee, M. Dell'Angela, A. Föhlisch, J. Gladh, T. Katayama, S. Kaya, O. Krupin, A. Møgelhøj, A. Nilsson, D. Nordlund, J.K. Nørskov, H. Öberg, H. Ogasawara, L.G.M. Pettersson, W.F. Schlotter, J.A. Sellberg, F. Sorgenfrei, J.J. Turner, M. Wolf, W. Wurth, H. Öström, Selective ultrafast probing of transient hot chemisorbed and precursor states of CO on Ru(0001), Phys. Rev. Lett. 110 (18) (2013) 186101.

[89] H. Tillborg, A. Nilsson, N. Mårtensson, J.N. Andersen, Adsorption-site-dependent X-ray-absorption spectroscopy - CO/H, H2/Ni(100), Phys. Rev. B 47 (3) (1993) 1699–1702.

[90] H. Tillborg, A. Nilsson, N. Mårtensson, Studies of the CO-H, H2-Ni(100) system using photoelectron-spectroscopy, Surf. Sci. 273 (1–2) (1992) 47–60.

[91] M. Bowker, The role of precursor states in adsorption, surface reactions and catalysis, J. Phys.-Cond. Matter 22 (26) (2010) 263002.

[92] M. Bowker, Role of precursors and lateral interactions in catalytic reactions at surfaces, Langmuir 7 (11) (1991) 2534–2538.

[93] H. Petek, Photoexcitation of adsorbates on metal surfaces: one-step or three-step, J. Chem. Phys. 137 (9) (2012) 091704.

[94] H. Petek, S. Ogawa, Surface femtochemistry: observation and quantum control of frustrated desorption of alkali atoms from noble metals, Ann. Rev. Phys. Chem. 53 (2002) 507–531.

[95] T.H. Her, R.J. Finlay, C. Wu, E. Mazur, Surface femtochemistry of CO/O-2/Pt (111): the importance of nonthermalized substrate electrons, J. Chem. Phys. 108 (20) (1998) 8595–8598.

[96] C. Bungaro, C. Noguera, P. Ballone, W. Kress, Early oxidation stages of Mg (0001): a density functional study, Phys. Rev. Lett. 79 (22) (1997) 4433–4436.

[97] J. Ghijsen, H. Namba, P.A. Thiry, J.J. Pireaux, P. Caudano, Adsorption of oxygen on the magnesium (0001) surface studied by XPS, Appl. Surf. Sci. 8 (4) (1981) 397–411.

[98] M. Morin, N.J. Levinos, A.L. Harris, Vibrational energy transfer of CO/Cu(100): nonadiabatic vibration/electron coupling, J. Chem. Phys. 96 (5) (1992) 3950–3956.

[99] M. Head-Gordon, J.C. Tully, Molecular-orbital calculations of the lifetimes of the vibrational-modes of CO on CU(100), Phys. Rev. B 46 (3) (1992) 1853–1856.

[100] S. Fleischer, Y. Zhou, R.W. Field, K.A. Nelson, Molecular orientation and alignment by intense single-cycle THz pulses, Phys. Rev. Lett. 107 (16) (2011).

[101] A. Huzayyin, J.H. Chang, K. Lian, F. Dawson, Interaction of water molecule with Au(111) and Au(110) surfaces under the influence of an external electric field, J. Phys. Chem. C 118 (7) (2014) 3459–3470.

[102] F. Djurabekova, S. Parviainen, A. Pohjonen, K. Nordlund, Atomistic modeling of metal surfaces under electric fields: direct coupling of electric fields to a molecular dynamics algorithm, Phys. Rev. E 83 (2) (2011) 026704.

[103] M.B. Partenskii, V.E. Kuzema, V.I. Fel'dman, Effects of an electric field on the surface electron barrier in a metal in the presence of an adsorbate. II. An improved Thomas-Fermi method, Sov. Phys. J. 24 (11) (1981) 985–989.

[104] J. Stöhr, F. Sette, A.L. Johnson, Near-edge X-ray-absorption fine-structure studies of chemisorbed hydrocarbons: bond lengths with a ruler, Phys. Rev. Lett. 53 (17) (1984) 1684–1687.
[105] Applications of Synchrotron Radiation, High Resolution Studies of Molecules and Molecular Adsorbates on Surfaces, Springer, Berlin, 1994.
[106] A. Nilsson, Applications of core level spectroscopy to adsorbates, J. Electron Spectrosc. Rel. Phenom. 126 (1–3) (2002) 3–42.
[107] M. Dell'Angela, T. Anniyev, M. Beye, R. Coffee, A. Föhlisch, J. Gladh, S. Kaya, T. Katayama, O. Krupin, A. Nilsson, D. Nordlund, W.F. Schlotter, J.A. Sellberg, F. Sorgenfrei, J.J. Turner, H. Öström, H. Ogasawara, M. Wolf, W. Wurth, Vacuum space charge effects in sub-picosecond soft X-ray photoemission on a molecular adsorbate layer, Struct. Dynam. 2 (2) (2015) 025101.
[108] J.J. Turner, G.L. Dakovski, M.C. Hoffmann, H.Y. Hwang, A. Zarem, W.F. Schlotter, S. Moeller, M.P. Minitti, U. Staub, S. Johnson, A. Mitra, M. Swiggers, P. Noonan, G.I. Curiel, M. Holmes, Combining THz laser excitation with resonant soft X-ray scattering at the linac coherent light source, J. Synchrot. Rad. 22 (2015) 621–625.

Anders Nilsson received a PhD in physics at Uppsala University, Sweden (1989) in the laboratory created by Kai Siegbahn. He is currently professor in Chemical Physics at Stockholm University and until 2016 was professor in Photon Science for 15 years at Stanford University. He received the Lindbomska Award at the Swedish Royal Academy of Science, the Royal Oscar Award at Uppsala University in 1994, the Shirley Award in Berkeley 1998, the Humboldt Award for senior scientist in 2010 and was awarded an honorary doctorate at Denmark Technical University in 2015. His research interests include synchrotron radiation and X-ray laser spectroscopy and scattering, chemical bonding and reactions on surfaces, ultrafast science heterogeneous catalysis, electrocatalysis in fuel cells, photocatalysis for converting sunlight to fuels, structure of water and aqueous solutions.

Jerry LaRue received his PhD in chemistry at the University of California, Santa Barbara in 2011 under Dr. Alec Wodtke. He is currently an Assistant Professor of Chemistry in the Schmid College of Science and Technology at Chapman University. His current research interests include using ultrafast optical techniques, X-ray spectroscopy, and Raman spectroscopy to study the fundamental bond making and breaking processes that occur during chemical reactions on catalytic surfaces.

Henrik Öberg did his PhD research in chemical physics at Stockholm University (2014) in the group of Professor Lars G.M. Pettersson. He continued as a postdoctoral researcher at Stockholm University before moving to the Department of Applied Physical Chemistry at KTH Royal Institute of Technology in Stockholm in 2015 to work as a researcher. He is currently working as an analyst at the Swedish Radiation Safety Authority. His research interests include quantum chemistry, chemical bonding on surfaces, reaction kinetics and dynamics, heterogeneous catalysis, X-ray spectroscopy, enzyme catalysis, metal corrosion.

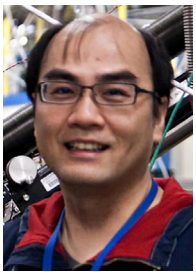

Hirohito Ogasawara earned his Ph.D. degree in chemistry in 1996 from Keio University, Japan, for his work on vibrational spectroscopic at electrolyte/electrode interfaces under the direction of Prof. Masatoki Ito. He spent seven years at RIKEN in Prof. Maki Kawai's group and five years in Prof. Anders Nilsson's group at Stockholm University and SLAC National Accelerator Laboratory. In 2006, he became a staff scientist at the Stanford Synchrotron Radiation Lightsource, SLAC National Accelerator Laboratory. His work is devoted to chemical process at surfaces and interfaces. Recent efforts focus developments in in-situ, operando and real-time spectroscopic investigations using synchrotron radiation and X-ray laser.

Martina Dell'Angela received a PhD in physics at University of Trieste, Italy (2009). She worked at ALOISA beamline of Elettra synchrotron (Trieste, Italy) studying the self-assembly on metal substrates of organic molecules relevant for electronics. Subsequently she has been post Doc at University of Hamburg/CFEL in the group of prof. Wilfried Wurth. She studied with time-resolved X-ray techniques ultrafast chemical reactions. Currently she is researcher at 'Istituto Officina Dei Materiali' (IOM) of the Italian National Research Council (CNR). She applies time resolved spectroscopies with synchrotrons and X-ray lasers to the study of reactions on surfaces and of photovoltaic materials.

Martin Beye received a PhD in physics at the University of Hamburg, Germany (2010) in the group of Wilfried Wurth. Later, he worked with Anders Nilsson at the SLAC National Accelerator Center in Stanford, USA and with Alexander Föhlisch, at the Helmholtz-Zentrum Berlin, Germany, partially funded through two fellowships from the Volkswagen foundation. He is currently a young investigator group leader at DESY in Hamburg, Germany. He develops new methods for synchrotron radiation and X-ray laser spectroscopy to study chemistry and dynamics on surfaces and in the liquid phase, as well as dynamics of phase transitions in condensed matter.

Henrik Öström received a PhD in physics at Stockholm University, Sweden (2004) in the groups of Anders Nilsson and Lars GM Pettersson on a thesis focusing on hydrocarbon interaction with metal surfaces. He then went to Martin Wolf at the Freie Universität, Berlin, venturing into the field of ultrafast surface science. He is currently an associate professor in chemical physics at Stockholm University building up a group with a focus on femtosecond chemistry on surfaces. His research includes ultrafast surface science, catalysis, synchrotron radiation surface spectroscopy, X-ray laser studies and optical lasers.

Jörgen Gladh received his Ph. Licentiate at Stockholm University, Sweden in 2012 and as Engineer in technical physics at Karlstad University in 2007. Currently he is working on his PhD thesis at Stockholm University. His research includes, chemical bonding on metal surfaces and reactions, ultrafast science, and heterogeneous catalysis, where he has worked with synchrotron radiation for core level spectroscopy, optical lasers and X-ray laser spectroscopy.

Jens Nørskov received his PhD in theoretical physics at the University of Aarhus, Denmark in 1979. Following his PhD he was a research fellow, post-doctoral researcher and staff scientist at several institutions including the Nordic Institute for Theoretical Physics, IBM T.J. Watson Research Center and Haldor Topsøe. In 1987 he joined the Technical University of Denmark as professor of physics. In 2010 he became a professor of Chemical Engineering and Photon Science and Director of the SUNCAT Center for Interface Science and Catalysis at Stanford University and SLAC National Accelerator Laboratory. Jens Nørskov's research aims at developing theoretical methods and concepts to understand and predict properties of materials. He is particularly interested in surface chemical properties, heterogeneous catalysis, electro-catalysis, and applications in energy conversion.

Wilfried Wurth received a PhD in physics from the Technical University Munich, Germany in 1987. He is currently scientific head of FLASH, the first XUV and soft X-ray free-electron laser world-wide operated as a user facility, at DESY in Hamburg and professor in experimental physics at the Center for Free-Electron Laser Science at the University of Hamburg. His research interests include linear and non-linear soft X-ray spectroscopy, free-electron laser physics and instrumentation for free-electron laser science, ultrafast dynamics in solids and at surfaces.

Frank Abild-Pedersen received his PhD in Physics at the Technical University of Denmark (2005). He currently holds a position as a Staff Scientist at the Center for Interface Science and Catalysis (SUNCAT) at SLAC National Accelerator Laboratory where his research focuses on developing theoretical models for molecule surface interactions and for understanding ultrafast surface processed measured by X-ray free electron lasers.

Lars G.M. Pettersson was born in Norrköping, Sweden in 1951 and received a BSc in physics (1976) and a PhD in theoretical physics (1984) from Stockholm University, Sweden, where he focused on highly accurate quantum chemical calculations as well as developing approximate modeling techniques. He did post-doctoral studies (1984-1986) in California at IBM, San Jose, and NASA Ames Research Center. He returned to Stockholm University where he is currently professor in theoretical chemical physics. He has published more than 300 scientific publications with focus on quantum chemical modeling of processes at surfaces, theoretical treatment and application of inner-shell spectroscopies. A major effort is currently devoted to understanding the structure and dynamics of water and aqueous solutions.